1 Inorganic and Bioinorganic Spectroscopy

EDWARD I. SOLOMON and CALEB B. BELL III

1.1 INTRODUCTION

Spectroscopic methods have played a critical and symbiotic role in the development of our understanding of the electronic structure, physical properties, and reactivity of inorganic compounds and active sites in biological catalysis.[1,2] Ligand field theory[3] developed with our understanding of the photophysical and magnetic properties of transition metal complexes. Ligand–metal (L–M) bonding descriptions evolved through the connection of π-donor interactions with ligand to metal charge transfer (LMCT) transitions and π-backbonding with metal to ligand charge transfer (MLCT) transitions.[4] X-ray absorption (XAS) spectroscopy initially focused on the use of extended X-ray absorption fine structure[5] (EXAFS) to determine the geometric structure of a metal site in solution, but evolved in the analyses of pre-edges and edges to probe the electronic structure and thus covalency of ligand–metal bonds.[6]

In bioinorganic chemistry, spectroscopy probes the geometric and electronic structure of a metallobiomolecule active site allowing the correlation of structure with function (Figure 1.1).[7]

Spectroscopies are also used to experimentally probe transient species along a reaction coordinate, where often the sample has been rapidly freeze quenched to trap intermediates. An important theme in bioinorganic chemistry is that active sites often exhibit unique spectroscopic features, compared to small model complexes with the same metal ion.[8] These unusual spectroscopic features reflect novel geometric and electronic structures available to the metal ion in the protein environment. These unique spectral features are low-energy intense absorption bands and unusual spin Hamiltonian parameters. We have shown that these reflect highly covalent sites (i.e., where the metal d-orbitals have significant ligand character) that can activate the metal site for reactivity.[9]

It is the goal of this chapter to provide an overview of the excited-state spectroscopic methods, including electronic absorption, circular dichroism (CD), magnetic
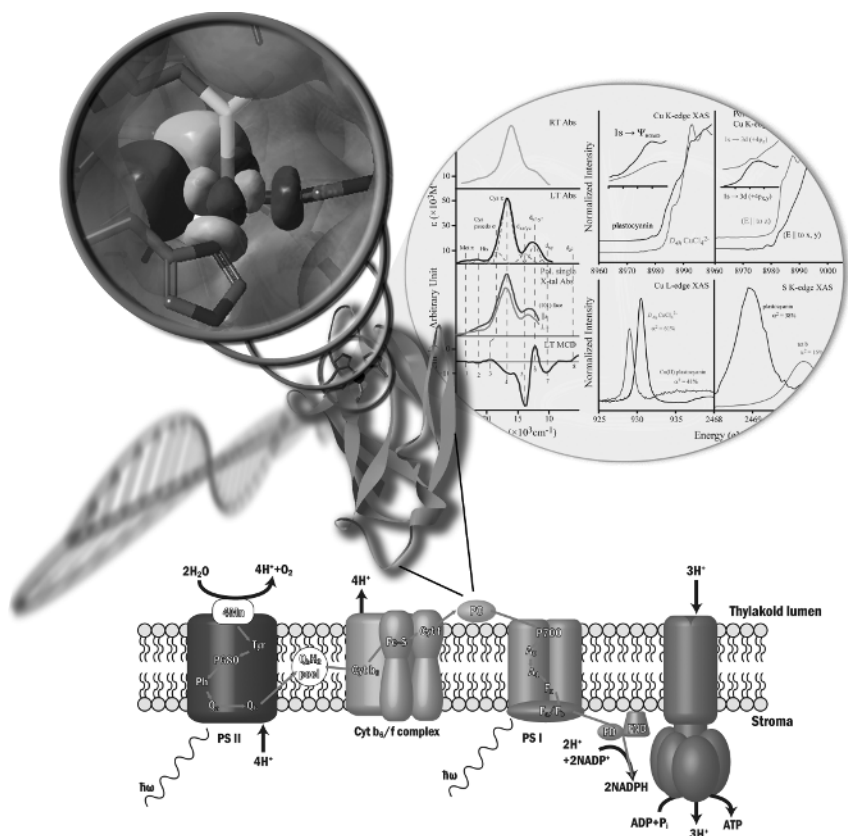
FIGURE 1.1   As an example, plastocyanin functions in photosynthesis as a soluble electron carrier in the thylakoid lumen transferring electrons from the cytochrome b_6/f complex to photosystem I ultimately for ATP synthesis (bottom). Despite its relatively small size, plastocyanin has had a large impact on the field of bioinorganic spectroscopy. The protein has a characteristic intense blue color (hence the term blue copper protein) that was later shown to derive from LMCT to the Cu. Hans Freeman first reported a crystal structure (light blue ribbon diagram, PDB ID, 1PLC) for plastocyanin in 1978[8] showing that the Cu site was tetrahedrally coordinated by a methionine, a cysteine, and two histidine resides. This was a surprising result given the typical tetragonal structure for small model Cu(II) complexes. Since that time, a tour de force of spectroscopy has been applied in blue copper research (projected on the back are selected spectra for methods that are covered in this chapter), many of which were developed and first used on this enzyme, as will be presented. The spectroscopic approach combined with electronic structure calculations has allowed elucidation of the geometric and electronic structures of the Cu site (top left blowup) that in turn has been used for structure–function correlations in understanding plastocyanin's biochemical role in electron transfer (ET) and defining the role of the protein in determining geometric and electronic structure. (See the color version of this figure in Color Plates section.)

circular dichroism (MCD), and X-ray absorption edge spectroscopies. Ground-state methods are presented in subsequent chapters and mostly focus on the first few wavenumbers (cm^{-1}) of the electronic structure of a transition metal site. Here we first consider ligand field (d → d) transitions in the near-IR to visible spectral region, from about 5000 to ~20,000 cm^{-1}, then charge transfer (CT) transitions in the visible to UV regions (up to ~32,000 cm^{-1} ~4 eV), and finally X-ray edge transitions that involve core excitations and energies up to 10^4 eV. We apply the concepts developed to two cases that generally define the information content of the method: the simple case of Cu(II) complexes with a d^9 one-hole configuration and the most complex case of Fe(III) d^5 complexes with a half-occupied valence configuration. It is important to emphasize that the rapid development of electronic structure calculations for transition metal systems, particularly density functional theory (DFT), has made a correlation to spectroscopy of critical importance.[10] There are many ways and levels of performing these calculations that can provide very different descriptions of bonding and reactivity. Spectroscopy experimentally defines the electronic and geometric structure of a transition metal site. Calculations supported by and combined with the experimental data can provide fundamental insight into the electronic structure and define this contribution to physical properties and the activation of a metal site for reactivity.

1.2   LIGAND FIELD (d → d) EXCITED STATES

1.2.1   Electronic Absorption Spectroscopy

In electronic absorption spectroscopy, we are interested in a transition from the ground state Ψ_g to an excited state Ψ_e that is allowed by the transition moment operator $\hat{M}$ that derives from the interaction of the electromagnetic radiation of the photon with the electron in a metal complex (Figure 1.2).
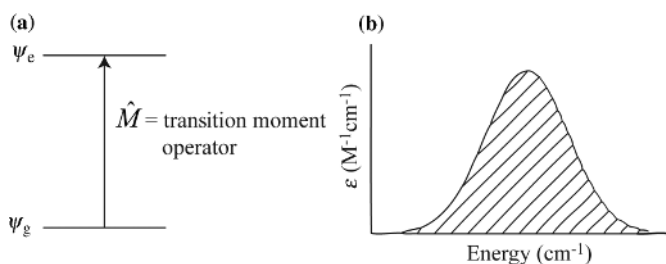
FIGURE 1.2   (a) The interaction of electromagnetic radiation with a metal center promotes an electron from the ground state (Ψ_g) to the excited state (Ψ_e) as dictated by the transition moment operator. This leads to the absorption band shape shown in (b).

This leads to an absorption band, and the quantity that connects experiment with theory is the oscillator strength of the transition, f.

$$f_{exp} = (4.33 \times 10^{-9}) \int \varepsilon(\upsilon)d\upsilon \qquad \upsilon \text{ in cm}^{-1}$$

$$f_{theo} = (1.085 \times 10^{11})\upsilon \left(\int \Psi_e^* \hat{M} \Psi_g d\tau \right)^2 \quad \text{transition moment integral in cm}^{-1}$$

$$(1.1)$$

Experimentally, the oscillator strength is given by the integrated intensity (area) under the absorption band, while theoretically it is given by the square of the transition moment integral $\int \Psi_g \hat{M} \Psi_e \, d\tau$. This leads to the selection rules for electronic transitions: when $\int \Psi_g \hat{M} \Psi_e \, d\tau$ is nonzero, there is absorption intensity and the transition is "allowed"; when this integral is required to be zero, the transition is "forbidden."

When the wavelength of light is much greater than the radius of the electron on the metal site (the long-wave approximation), the transition moment operator is given by the multipole expansion:[11]

$$\hat{M} = \hat{M}_{\text{(electric dipole)}} + \hat{M}_{\text{(magnetic dipole)}} + \hat{M}_{\text{(electric quadrupole)}} + \cdots \qquad (1.2)$$

where each term in the expansion is $\sim 10^3$ times more effective than the subsequent term. Note that green light has $\lambda \sim 5000$ Å, while the radius of an electron in transition metal complexes is on the order of a few angstroms. For electronic absorption spectroscopy, we are interested in the dominant, electronic dipole term, where $\hat{M}_{\text{(electric dipole)}} = e\vec{r} \cdot \vec{E}$. The electric vector of light ($\vec{E}$) projects out a specific component of $\vec{r}$, which operates on the electron coordinates in the transition moment integral in Equation 1.1.

Note that, since the electric dipole operator does not involve the electron spin, the transition moment integral $\int \Psi_g \hat{M}_{\text{electric dipole}} \Psi_e \, d\tau$ is nonzero only if Ψ_g and Ψ_e have the same spin leading to the selection rule $\Delta S = 0$ for a "spin-allowed" transition. For electronic absorption spectroscopy in the ligand field region, we focus on excitation of electrons between a ligand field split set of d-orbitals. Since d-orbitals are symmetric (gerade or g) to inversion and the electric dipole operator $\vec{r} = x, y, z$ is antisymmetric to inversion (ungerade or u), all d $\rightarrow$ d transitions are forbidden due to the total u symmetry of the integral; these are called "parity" or "Laporte" forbidden transitions. However, metal sites in proteins and low-symmetry complexes have no inversion center; therefore, the d $\rightarrow$ d transitions become weakly allowed through mixing with higher energy electric dipole-allowed charge transfer transitions (see below). This leads to molar extinction coefficients (ε) of up to a few 100 $M^{-1} cm^{-1}$ for spin-allowed d $\rightarrow$ d transitions. It is important to note that metalloprotein solutions of ~ 1 mM in a 1 mm cuvette will give an absorbance of ~ 0.01, which is difficult to observe experimentally. This is particularly the case for d $\rightarrow$ d transitions that occur at relativity low energy as given by ligand field theory.
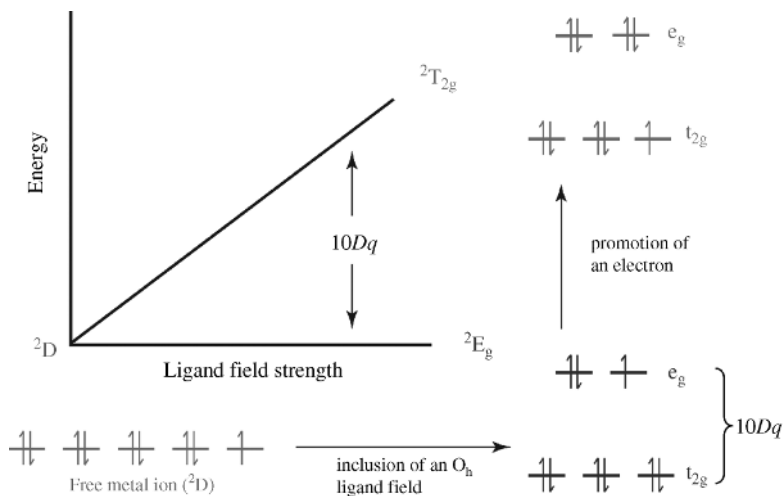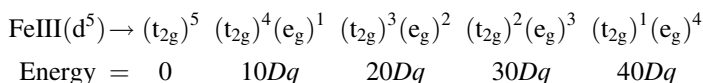
FIGURE 1.3 Effects of a ligand field (LF) on a Cu(II) d^9 ion and the corresponding Tanabe–Sugano diagram. The electron configurations leading to each state are shown.

1.2.1.1 *Ligand Field Theory of Cu(II) d^9 and Fe(III) d^5 Ions*
The ligand field ground and excited states of a d^n transition metal complex are given by the Tanabe–Sugano diagrams,[12] which quantitatively define the effects of the ligand field splittings of the d-orbitals on the many-electron atomic term symbols of the free metal ion.

As shown in Figure 1.3, the Cu(II) d^9 free ion has one hole in the fivefold degenerate set of d-orbitals giving a ^2D atomic term symbol. In an octahedral (O_h) ligand field, the d-orbitals are split in energy into the t_{2g} and e_g orbital sets, by $10Dq$, the spectroscopic parameter of ligand field theory. It should be mentioned that in the original derivation by Bethe, D parameterized the crystal field electrostatic distribution and q a radial integral over the d-orbitals.[13] Now these are considered as one parameter obtained experimentally by correlating the Tanabe–Sugano diagram splittings to the experimentally observed transition energies. For a d^9 Cu(II) ion in an octahedral ligand field, this gives a $t_{2g}^6 e_g^3$ electron configuration, thus giving a ^2E_g ground state with a $t_{2g}^5 e_g^4$ or $^2T_{2g}$ first excited state at $10Dq$. The Tanabe– Sugano diagram for this simple one-hole case is shown in Figure 1.3; the ^2D splits into two states, ^2E_g and $^2T_{2g}$, with the energy separation increasing with $10Dq$.

For Fe(III), there are five valence electrons that generate the following configurations when distributed over an O_h ligand field split set of d-orbitals:

$$\text{FeIII}(d^5) \rightarrow (t_{2g})^5 \quad (t_{2g})^4(e_g)^1 \quad (t_{2g})^3(e_g)^2 \quad (t_{2g})^2(e_g)^3 \quad (t_{2g})^1(e_g)^4$$
$$\text{Energy} = \quad 0 \qquad 10Dq \qquad 20Dq \qquad 30Dq \qquad 40Dq$$

For each of these configurations, one must also consider electron–electron repulsions that split each configuration into a number of ligand field states that can further interact with each other, through configuration interaction (CI), leading to the Tanabe–Sugano diagram of the d^5 configuration given in Figure 1.4.
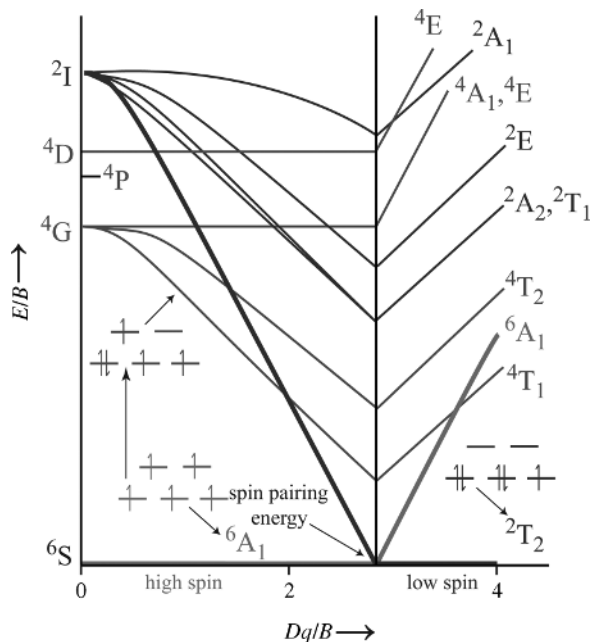
FIGURE 1.4 Tanabe-Sugano diagram for a d^5 ion. Insets are the d electron configurations for the indicated states. (See the color version of this figure in Color Plates section.)

Here the energy units are in B (cm^{-1}), where B is the Racah parameter[14] that quantitates electron–electron repulsion, obtained experimentally for a given free metal ion and allowed to reduce due to covalency (i.e., the nephelauxetic effect[15]). The left-hand side of Figure 1.4 represents the high-spin $t_{2g}{}^3 e_g{}^2$ ($^6A_{1g}$) ground state, while the right-hand side represents the low-spin $t_{2g}{}^5$ ($^2T_{2g}$) ground state. The crossing point at $Dq/B = 2.8$ quantitates the ligand field splitting of the d-orbitals required to overcome the electron–electron repulsion (i.e., $t_{2g}{}^3 e_g{}^2 \leftrightarrow t_{2g}{}^5 e_g{}^0$), which is defined as the spin-pairing energy for this configuration. In the inset on the left-hand side of Figure 1.4, the lowest energy ligand field excited state on the high-spin side of the d^5 Tanabe–Sugano diagram ($^4T_{1g}$) corresponds to an $e_g(\uparrow) \rightarrow t_{2g}(\downarrow)$ transition. This is an excited state due to the increased electron–electron repulsion relative to the energy splitting of the t_2 and e sets of d-orbitals. The transition to the $^4T_{1g}$ from the $^6A_{1g}$ ground state is spin forbidden. In fact, all d $\rightarrow$ d transitions for high-spin Fe(III) are $\Delta S = 1$ (or 2); therefore, they are spin forbidden and will not have significant intensity in the absorption spectrum (generally $\varepsilon < 0.1\,M^{-1}\,cm^{-1}$).

Alternatively, for d^9 Cu(II) complexes from Figure 1.3, the $^2E_g \rightarrow {}^2T_{2g}$ transition at $10Dq$ is spin allowed. For divalent first transition row metal ions with biologically relevant ligands, $10Dq$ is in the range of $10{,}000$–$12{,}000\,cm^{-1}$; therefore, transitions are expected in the near-IR spectral region. Both the ground and excited states are orbitally degenerate and will split in energy in a characteristic way depending on the geometry of the Cu(II) site.
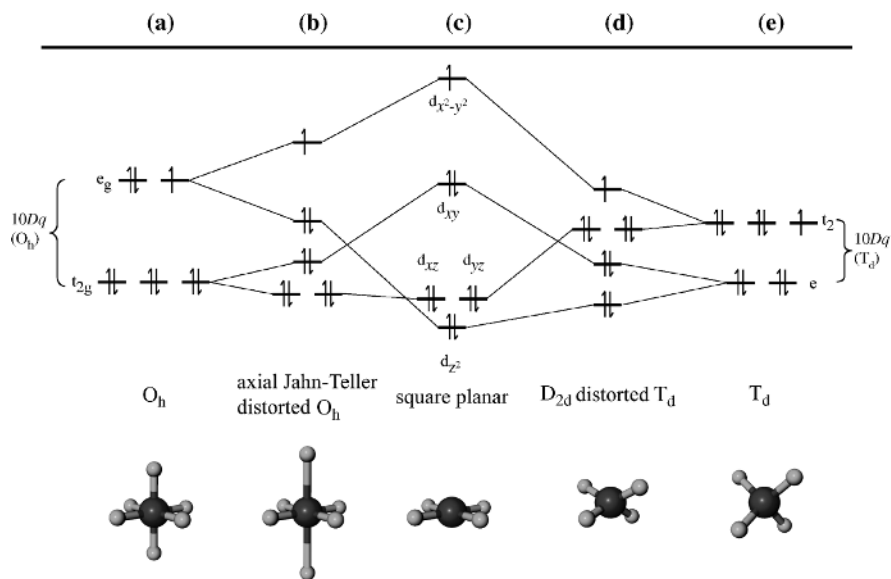
FIGURE 1.5 Splitting of metal 3d orbitals in various ligand field environments.

1.2.1.2 Geometric Dependence of Spin-Allowed Ligand Field Transitions

Ligand field theory quantitates the splittings of the one-electron d-orbitals due to their repulsion/antibonding interactions with the ligands.

As shown in Figure 1.5a for d^9 Cu(II) ions in an O_h ligand field, the ground configuration (and state) is $t_{2g}^6 e_g^3$ (^2E_g). The extra electron in the e_g set of d-orbitals is strongly σ-antibonding with the ligands, and this interaction is anisotropic. Thus, the orbital degeneracy of the ground state leads to a Jahn–Teller distortion[16] of the ligand field to lower the symmetry, splits the e_g orbital degeneracy, and lowers the energy of the d^9 complex. Generally, Cu(II) complexes are found to have a tetragonal elongated structure (Figure 1.5b) or, in the limit of loss of the axial ligands, a square planar structure (Figure 1.5c). Note from Figure 1.5 that the ligand field splittings of the d-orbitals greatly change for the square planar relative to the O_h limit due to differences in antibonding interactions of the metal ion with the ligands in a square planar versus an O_h ligand field.

A geometric distortion that has been of considerable interest in inorganic and bioinorganic chemistry is the square planar (D_{4h}) to D_{2d} distorted to tetrahedral (T_d) limit[17] (Figure 1.5c–e). From the energy levels in Figure 1.5, the ligand field transitions go down in energy from the 12,000 cm^{-1} region to the 5000 cm^{-1} region across the series. This reflects the prediction of ligand field theory that $10Dq$ of a T_d complex is $-4/9$ $10Dq$ of the corresponding O_h complex. As depicted in Figure 1.5, the ligand field transition energies are a sensitive probe of the geometry of the Cu(II) site. However, these are in the 12,000–5000 cm^{-1}, near-IR, spectral region that can have intense contributions from protein, buffer, and H_2O vibrations to the absorptions

spectrum. In addition, due to their parity forbiddeness (i.e., low intensity), these $d \rightarrow d$ transitions generally are not experimentally observed in the absorption spectra of proteins. However, based on the different selection rules associated with different spectroscopies, these transitions can be very intense in circular dichroism and magnetic circular dichroism spectroscopies in the near-IR spectral region.

1.2.2 Circular Dichroism Spectroscopy

CD spectroscopy measures, with high sensitivity using modulation and lock-in detection, the difference in the absorption of left (L) and right (R) circularly polarized (CP) light (the direction of rotation of the $\vec{E}$ vector as light propagates toward the observer) in a transition between the ground and excited states ($\Psi_g \rightarrow \Psi_e$). The spectrum is plotted as $\Delta\varepsilon = \varepsilon_L - \varepsilon_R$ versus energy, and since CD has a sign as well as a magnitude, it can often resolve overlapping bands in a broad absorption envelope, as illustrated in Figure 1.6.

The quantity that connects theory with experiment in CD spectroscopy is the rotational strength R. On an experimental level, R is determined by the area under a resolved CD transition (Figure 1.6b), while from theory the rotational strength is proportional to the projection of the electric dipole moment of a $\Psi_g \rightarrow \Psi_e$ transition
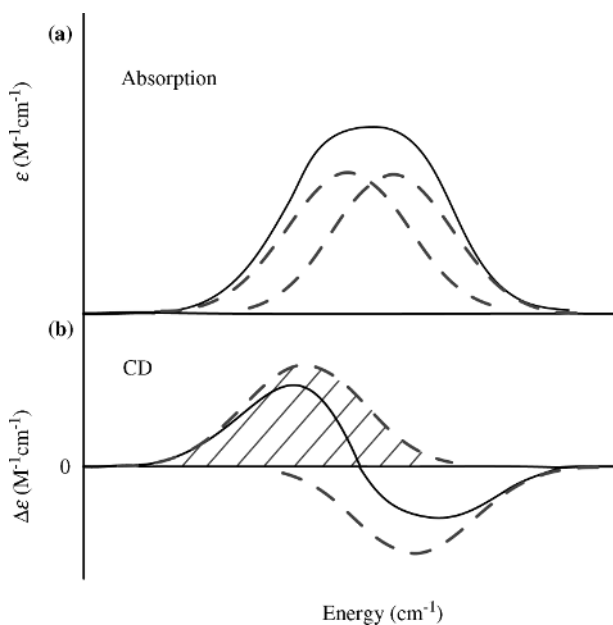
FIGURE 1.6   Schematic representation of the resolution of an absorption envelope by CD spectroscopy, due to the sign of CD transitions. Shaded area indicates R-value of a given transition in CD.

onto its magnetic dipole moment (Equations 3a and 3b, respectively):[18]

$$R_{\text{exp}} = 22.9 \times 10^{-40} \int \frac{\Delta\varepsilon}{\nu} d\nu \tag{1.3a}$$

$$R_{\text{theory}} = 4.7 \times 10^{-24} \, \text{Im} \int \Psi_g \hat{M}_{\text{electric dipole}} \Psi_e \, d\tau \cdot \int \Psi_g \hat{M}_{\text{magnetic dipole}} \Psi_e \, d\tau \tag{1.3b}$$

This form derives from the fact that circularly polarized light excites electrons in a helical motion, requiring the electronic excitation to undergo both translational (electric dipole (x, y, z)) and rotational (magnetic dipole (R_x, R_y, R_z)) operations. Note from Equation 3b that only optically active molecules (point groups, C_n, D_n, or C_1 for a protein active site) can have a nonzero projection of the electric dipole and magnetic dipole moments for a given $\Psi_g \rightarrow \Psi_e$ transition (i.e., this transition must be allowed by the same component of $\hat{M}(x, y, z)$ and $\hat{R}(x, y, z)$; therefore, $\hat{M}_i$ and $\hat{R}_i$ must transform as the same irreducible representation in the point group of the molecule).

Generally electronic transitions are electric dipole allowed or gain electric dipole character through low-symmetry site distortions such as in a protein active site; therefore, the magnetic dipole operator dominates the rotational strength. $\hat{M}_{\text{(magnetic dipole)}}$ in Equation 1.2 is given by $\beta\hat{L}\cdot\vec{H}$, where the $\vec{H}$ vector of light projects out a specific component of $\hat{L}_{i(i=x,y,z)}$. Again, Ψ_g and Ψ_e must have the same spin to be magnetic dipole allowed (leading to the selection rule $\Delta S = 0$) as $\hat{M}_{\text{(magnetic dipole)}}$ does not affect the spin part of the wavefunction.

We now consider the spin-allowed ligand field transitions of optically active Cu(II) complexes. The table below gives the effect of the $\hat{L}_i$ operator on electrons in d-orbitals.[3]

$\hat{L}_x d_{xz} = -id_{xy}$	$\hat{L}_y d_{xz} = -id_{x^2-y^2} - i\sqrt{3}d_{z^2}$	$\hat{L}_z d_{xz} = id_{yz}$
$\hat{L}_x d_{yz} = i\sqrt{3}d_{z^2} + id_{x^2-y^2}$	$\hat{L}_y d_{yz} = id_{xy}$	$\hat{L}_z d_{yz} = -id_{xz}$
$\hat{L}_x d_{xy} = id_{xz}$	$\hat{L}_y d_{xy} = -id_{yz}$	$\hat{L}_z d_{xy} = -2id_{x^2-y^2}$
$\hat{L}_x d_{x^2-y^2} = -id_{yz}$	$\hat{L}_y d_{x^2-y^2} = -id_{xz}$	$\hat{L}_z d_{x^2-y^2} = 2id_{xy}$
$\hat{L}_x d_{z^2} = -i\sqrt{3}d_{yz}$	$\hat{L}_y d_{z^2} = i\sqrt{3}d_{xz}$	$\hat{L}_z d_{z^2} = 0$

From Figure 1.5, many Cu(II) complexes have one hole in the $d_{x^2-y^2}$ orbital and $\hat{L}_z$ will allow the ligand field excitation of a d_{xy} electron into this hole, while $\hat{L}_x$ and $\hat{L}_y$ will allow magnetic dipole excitation of the d_{yz} and d_{xz} electrons into the $d_{x^2-y^2}$ orbital. In general, d → d (ligand field) transitions will be magnetic dipole allowed, have significant rotational strength, and appear with reasonable intensity in the CD spectrum.

It is common to define the Kuhn anisotropy factor, $g = \Delta\varepsilon/\varepsilon$, which is the intensity of a given $\Psi_g \rightarrow \Psi_e$ transition in the CD relative to the absorption spectrum. For reasonable values of f and R, it is generally found that g (not to be confused with the EPR g-values) > 0.01 for magnetic dipole-allowed transitions.[19]

From the above, d → d transitions in the near-IR spectral region will be moderately intense in CD, while vibrations of the protein and solvent will not, allowing CD

to be used as a sensitive probe of the ligand field of the metal site in a low-symmetry (e.g., protein) environment. Alternatively, CT transitions (see below) generally involve excitation of an electron from a donor to acceptor orbital along a bond. These will be intense in absorption but not in the CD spectrum; therefore, CT transitions will generally have low g-values, allowing one to distinguish between ligand field and CT transitions in spectral assignments.

Finally, it should be noted that $\hat{L}$ is a rotational operator. Therefore, any type of transition that involves exciting an electron between orbitals that are transformed into one another by a rotation (e.g., the $n \rightarrow \pi^*$ transition of an inherently chiral carbonyl)[20,21] will be magnetic dipole allowed and have $g \geq 0.01$.

1.2.3 Magnetic Circular Dichroism Spectroscopy

As its name implies, MCD spectroscopy involves taking a CD spectrum in a longitudinal magnetic field (i.e., $\vec{H}$ parallel to the propagation direction of the circularly polarized light).[22] In contrast to CD, which depends on the chirality at the metal due to a distorted environment, MCD spectroscopy directly probes the Zeeman splittings of the ground and excited states and the magnetic field-induced mixing between states.

A physical picture of the MCD effect is first presented by considering the simplest case of a complex having ground and excited states with angular momenta $J = 1/2$ ($M_J = \pm 1/2$) in Figure 1.7.

Application of a magnetic field leads to a Zeeman splitting of the ground- and excited-state doublets by $g_i \beta H$ (β is the Bohr magneton, H is the magnetic field, and the g_i value defines the Zeeman splitting in the ith direction and reflects the angular momentum in that state). EPR probes this splitting in the ground state (Chapter 3).
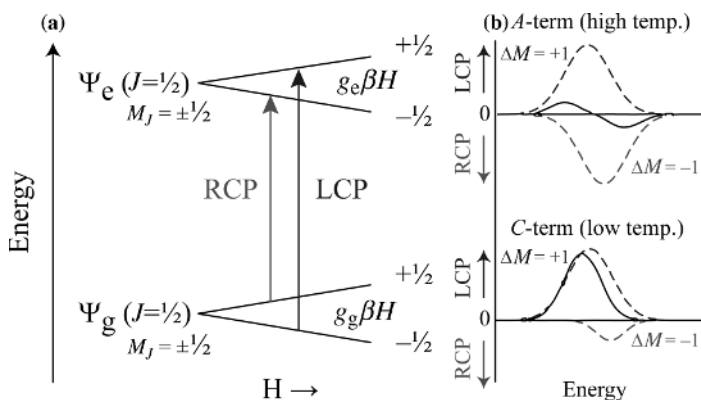

FIGURE 1.7 Panel (a) shows the Zeeman effect on degenerate ground and excited states caused by the application of a magnetic field (H). Panel (b) shows the A- and C-terms that result from the absorption of left and right circularly polarized light (LCP and RCP).

In MCD, we are interested in transitions between the ground and excited states where the selection rules for circularly polarized transitions are $\Delta M = +1$ for LCP light and $\Delta M = -1$ for RCP light. From Figure 1.7a, this leads to two transitions between the ground and a given excited state of equal magnitude but opposite sign. Since the Zeeman splittings are on the order of $10\,\text{cm}^{-1}$ (at fields up to $7-8\,\text{T}$ used in the MCD experiment) and electronic transitions in metal complexes are typically $\sim 1000\,\text{cm}^{-1}$ broad, these will mostly cancel and give a broad, weak derivative shaped feature (Figure 1.7b, top, where the resultant feature is the sum of the two dashed band shapes), known as an *A*-term. *A*-term features are independent of temperature, but depend on the *g*-values of the ground and excited states, at least one of which must be degenerate for *A*-term MCD intensity.[23] In this example, the *A*-term is observed when the temperature is high relative to the Zeeman splitting of the ground state. As temperature is lowered, the Boltzmann population of the higher energy component of the ground doublet decreases, eliminating the cancellation of the opposing circularly polarized band. This leads to an absorption band shaped feature that increases in intensity as temperature is lowered and is defined as a *C*-term (Figure 1.7b, bottom). The *C*-term depends on the *g*-value of the ground state, which must be degenerate in the absence of a magnetic field. Note that at low temperatures and high fields, the *C*-term intensity "saturates," which will be discussed in Section 1.2.3.2.

A- and *C*-terms require that either or both the ground and excited states must be degenerate. A *B*-term signal can occur when both states are nondegenerate, but there is an additional nondegenerate state (Ψ_k) that can mix with either due to the applied magnetic field. Figure 1.8a illustrates the effect of Ψ_k on the excited state (Ψ_e).

The magnetic field induces an MCD signal from the $\Psi_g \rightarrow \Psi_e$ transition that has the absorption band shape. This *B*-term is independent of temperature since the ground state is not Zeeman split (i.e., no state to Boltzmann populate) and increases in
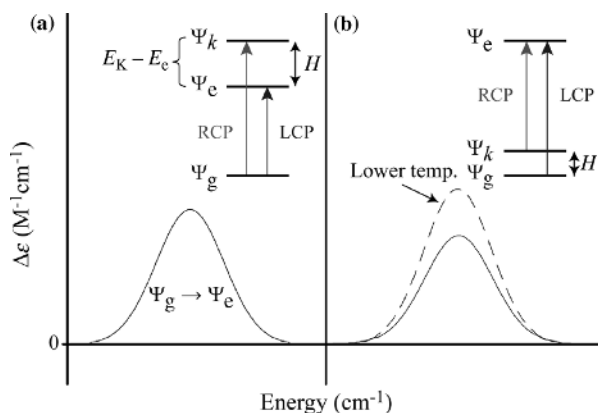
FIGURE 1.8 *B*-term intensity mechanism. Panel (a) shows the effect of Ψ_k on the excited state (Ψ_e) and panel (b) shows the effect of Ψ_k mixing into the ground state (Ψ_g) to produce the temperature dependent *B*-term MCD signal.

magnitude as $E_k - E_e$ decreases. Figure 1.8b shows the effect of field-induced mixing of Ψ_k into the ground state. The field induces circularly polarized intensity of equal magnitude but opposite sign for the transitions $\Psi_g \to \Psi_e$ and $\Psi_k \to \Psi_e$. If Ψ_k is low enough in energy to be thermally populated, this will lower the magnitude of the *B*-term signal. This special case produces a temperature-dependent *B*-term that often occurs when there is zero-field splitting (ZFS) (see Section 1.2.3.2). Finally, field-induced mixing of Ψ_k into Ψ_e leads to equal but opposite signed transitions to each of these excited states from the ground state. If the excited states are close in energy, this produces a temperature-independent derivative shaped feature known as a "pseudo *A*-term" composed of equal but opposite signed *B*-terms. It will be shown in Section 1.2.3.1 that there is also a pseudo *A*-term deriving from oppositely signed *C*-terms due to spin–orbit coupling. This, however, can be differentiated from the pseudo *A*-term described above because it will be temperature dependent.

The formalism developed by Buckingham and Stephens[23] for the *A*-, *B*-, and *C*-terms is given in Equation 1.4, where $f(E)$ is the absorption band shape (i.e., a Gaussian) and $\partial \mathbf{f}(E)/\partial E$ is its derivative.

$$\frac{\Delta A}{E} = \frac{2N_0\pi^3 a^2 Cl \log e}{250 hcm} \beta H \left[\mathbf{A}_1 \left(\frac{-\partial \mathbf{f}(E)}{\partial E} \right) + \left(\mathbf{B}_0 \frac{\mathbf{C}_0}{kT} \right) \right] f(E) \qquad (1.4)$$

The $\mathbf{A}_1$, $\mathbf{B}_0$, and $\mathbf{C}_0$ are the *A*-, *B*-, and *C*-term intensities, which are all linear in $\vec{H}$ and the *C*-term magnitude is proportional to $1/T$, when $kT \gg g\beta H$, defined as the "linear limit" (see Section 1.2.3.2). The "0" and "1" subscripts refer to the zero and first moments, which eliminate the effect of the band shape. The quantum mechanical expressions for these are given in Equation 1.5 for an applied field parallel to the molecular *z*-axis.[22,23]

$$\mathbf{A}_1 = \frac{1}{d_g} \sum \left(\langle e|L_z + 2S_z|e \rangle - \langle g|L_z + 2S_z|g \rangle \right) \times \left(|\langle g|M_-|e \rangle|^2 - |\langle g|M_+|e \rangle|^2 \right)$$

$$(1.5a)$$

$$\mathbf{B}_0 = \frac{2}{d_g} \mathrm{Re} \sum \left[\begin{array}{l} \displaystyle\sum_{K(K \neq e)} \frac{\langle e|L_z + 2S_z|K \rangle}{\Delta E_{Ke}} [\langle g|M_-|e \rangle \langle K|M_+|g \rangle - \langle g|M_+|e \rangle \langle K|M_-|g \rangle] \\[3mm] + \displaystyle\sum_{K(K \neq g)} \frac{\langle K|L_z + 2S_z|g \rangle}{\Delta E_{Kg}} [\langle g|M_-|e \rangle \langle e|M_+|K \rangle - \langle g|M_+|e \rangle \langle e|M_-|K \rangle] \end{array} \right]$$

$$(1.5b)$$

$$\mathbf{C}_0 = -\frac{1}{d_g} \sum \langle g|L_z + 2S_z|g \rangle \times \left(|\langle g|M_-|e \rangle|^2 - |\langle g|M_+|e \rangle|^2 \right) \qquad (1.5c)$$

Here d_g is the degeneracy of the ground state, $\mathbf{A}_1$ becomes $\mathbf{C}_0$ when only the ground state is degenerate, and the first contribution to $\mathbf{B}_0$ corresponds to field-induced

mixing of Ψ_k into the excited state and the second corresponds to field-induced mixing of Ψ_k into the ground state.

1.2.3.1   *Information Content of C-Terms*

Generally A- and B-terms are much weaker than C-terms for a paramagnetic center, particularly at cryogenic (i.e., liquid He) temperatures where C-terms are two to three orders of magnitude more intense. So the focus of this chapter is on C-terms arising from paramagnetic transition metal sites. Equation 5c can be written in a simplified form (Equation 1.6, which accounts for all orientations of $\vec{H}$ relative to the molecular z-axis),[24] where $M_{\pm 1} = \frac{1}{\sqrt{2}}(M_x \pm iM_y)$, g_i is the g_i-value of the ground state in the direction indicated, and M_i are the components of the electric dipole transition moment for $\Psi_g \to \Psi_e$. More important, this expression requires two perpendicular transition moments. However, for most metal centers, particularly in metalloproteins, the ground and excited states will be orbitally nondegenerate; therefore, the transition moment to each state can only be in one direction. Thus, C-term MCD intensity requires spin–orbit coupling between excited states with transition moments from the ground state in different directions.[25] This will mix some $M_{j\neq i}$ into a M_i polarized transition and result in C-term intensity (Equation 1.6).

$$\mathbf{C}_0 \propto g_z M_x M_y + g_y M_x M_z + g_x M_y M_z \qquad (1.6)$$

If any two excited states spin–orbit couple with each other, this will lead to equal and opposite signed C-terms (i.e., the temperature-dependent pseudo A-term, alluded to above). If more excited states are mixed by spin–orbit coupling, this leads to the "sum rule" where the total positive and negative MCD intensity over the full spectrum sums to zero.[26] If there is a large deviation from this (i.e., more C-term intensity over the spectrum in one circular polarization), it likely reflects spin–orbit coupling of a low-lying excited state, though thermally inaccessible, with the ground state.

An important point of the above discussion is that C-term MCD intensity requires spin–orbit coupling between excited states. The one-electron spin–orbit parameters of transition metal ions are generally much larger than those of the ligands ($\xi\text{Cu(II)} = 830\,\text{cm}^{-1}$ and $\xi\text{Fe(III)} = 460\,\text{cm}^{-1}$, relative to $\xi\text{O,N} \approx 60\text{–}70\,\text{cm}^{-1}$ and $\xi\text{S} = 325\,\text{cm}^{-1}$). Therefore, excited states with significant d character will be more spin–orbit mixed than ligand-based CT transitions and show much larger MCD relative to absorption intensity. This is quantified by the C_0/D_0 ratio where the dipole strength is given by $D_0 = 1/d_g \sum |\langle g|M|e\rangle|^2$ and equates to the electric dipole transition moment integral in Equation 1.1.

In summary, d → d transitions are characterized by high C_0/D_0 ratios (~0.1, an intense low-temperature MCD signal relative to a weak absorption signal), while CT transitions are intense in absorption (see below), relatively weak in low-temperature MCD, and thus have low C_0/D_0 ratios (~0.01). Finally, it should be noted that the sign and magnitude of the C_0/D_0 ratio can be used to make specific assignments of bands based on electronic structure calculations[27] (or group theory if there is high symmetry),[28] which include spin–orbit coupling.
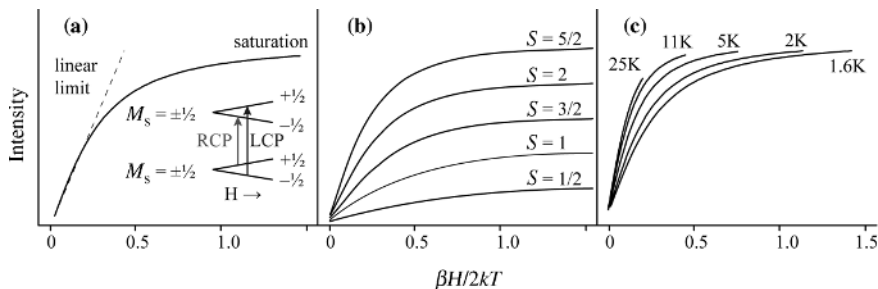
FIGURE 1.9   Saturation magnetization behavior of C-term MCD intensity. Panel (a) shows the linear and saturation limits of the intensity with the Zeeman effect on an $S = 1/2, M_S = \pm 1/2$ ground and excited states. Panel (b) shows the change of VTVH MCD behavior with S total. Panel (c) shows the nesting behavior observed for $S > 1/2$ with ZFS.

1.2.3.2   Saturation Magnetization: Variable-Temperature Variable-Field MCD
The variable-temperature variable-field (VTVH) MCD experiment is performed by sitting on an MCD peak maximum and increasing field (H) at fixed temperatures (T).[24,29,30] This is repeated for various temperatures and the data are plotted as a function of $\beta H/2kT$, where β is the Bohr magneton and k is the Boltzmann constant. This generates a set of saturation magnetization curves as shown in Figure 1.9c.

Initially, when the temperature is decreased and magnetic field increased, the MCD intensity increases linearly in the saturation magnetization curve (dashed line in Figure 1.9a for a spin 1/2 system at relatively low values of $\beta H/2kT$). However, at low temperatures and high magnetic fields, the magnetization curve saturates, and the MCD signal intensity becomes independent of T and H (saturation region in Figure 1.9a). The origin of this behavior can be understood from the inset in Figure 1.9a. At low temperatures and high fields, only the $M_S = -1/2$ component of the ground doublet is populated and at this value of $\beta H/2kT$, the MCD signal can no longer increase. From Figure 1.9b, as the spin of the ground state increases, the rate of achieving saturation increases, a behavior described by the Brillion function given by Equation 7 that can be used to obtain the spin (S) of the ground state.[31]

$$M = \tfrac{1}{2}Ng\beta \tanh(g\beta H/2kT), \quad \text{for } S = 1/2 \tag{1.7a}$$

$$M = NgS\beta B_s(x)$$

$$B_s(x) = \frac{2S+1}{2S}\coth\left(\frac{2S+1}{2S}\right) - \frac{1}{2S}\coth\left(\frac{1}{2S}x\right), \quad \text{for } S > 1/2 \tag{1.7b}$$

$$x = gS\beta H/2kT$$

It should be emphasized that the Brillion functions require that data taken at different temperatures and fields superimpose onto a single curve when plotted as a function of $\beta H/2kT$. This does occur for Cu(II) and other $S = 1/2$ complexes but is generally not

the case for $S > 1/2$ systems, where from Figure 1.9c curves obtained by increasing field at different fixed temperatures spread to form a nested set of saturation magnetization curves (or isotherms). This is due to zero-field splitting.

When $S > 1/2$ and the metal site symmetry is lower than O_h or T_d, there is a term in the spin Hamiltonian, in addition to the Zeeman term ($g_i\beta H$), that will split the $(2S + 1)$ M_S spin degeneracy even in the absence of a magnetic field.[32] This is shown in Equation 1.8, where D in the first term describes the effect of an axial distortion of the ligand field ($z \neq x = y$) and E in the second term accounts for the presence of a rhombic ligand field ($z \neq x \neq y$).

$$H = D\left(S_z^2 - 1/3 S^2\right) + E\left(S_x^2 - S_y^2\right) + \beta\left(g_x H_x S_x + g_y H_y S_y + g_z H_z S_z\right) \quad (1.8)$$

This will have a very different effect on the VTVH MCD data depending on whether the complex is a Kramers (odd number of electrons, half-integer spin) or non-Kramers (even number of electrons, integer spin) ion.[33]

Kramers Ions: The High-Spin Fe(III) $S = 5/2$ Case   The effects of the ZFS and Zeeman terms in Equation 1.8 on an $S = 5/2$ ground state are shown in Figure 1.10 for a rhombic Fe(III) site with $D > 0$. First, note that the sixfold degenerate M_S values of
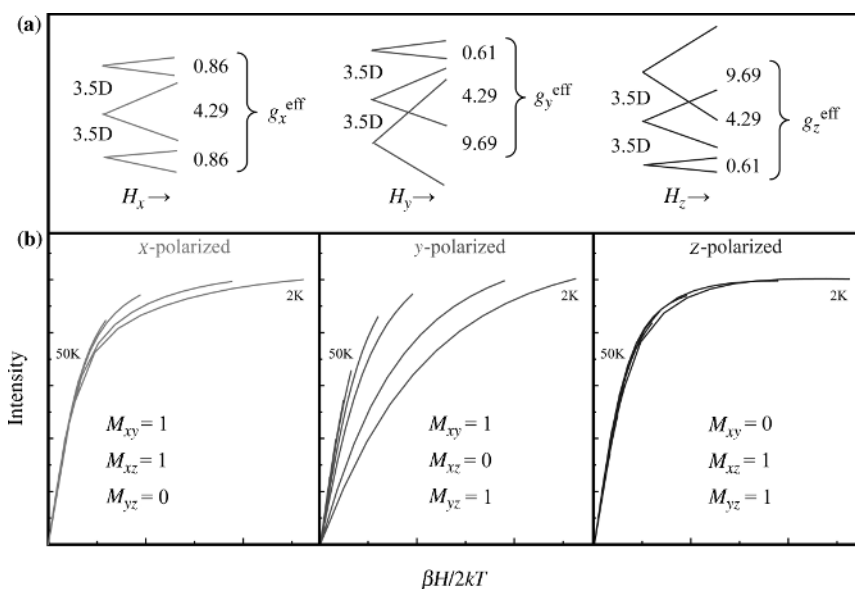
FIGURE 1.10   Panel (a) shows the effect of ZFS (left side) and application of a magnetic field in three molecular directions on the spin states giving rise to the observed saturation magnetization behavior (VTVH MCD) plotted in panel (b) for a $S = 5/2$, $D > 0$, and $E/D = 1/3$ Kramers ion.

the $S = 5/2$ ground state split into three doublets in the absence of a magnetic field (left-hand side of Figure 1.10a).

Kramers' theorem requires that all half-integer spin systems be at least doubly degenerate in the absence of a magnetic field. Next, note that the splitting of these levels by a magnetic field depends on its orientation relative to the axes of the ZFS tensor of the metal ion. The VTVH MCD saturation magnetization curve behavior reflects the difference in the population of these levels and their spin expectation values in a specific molecular direction. This direction must be perpendicular to the polarizations of the transition (M_{ij}, where $i \neq j$ are the two perpendicular polarizations required for circular polarization) (Equation 1.9).[27]

$$\frac{\Delta\varepsilon}{E} = \frac{\gamma}{4\pi S} \int_0^\pi \int_0^{2\pi} \sum_i N_i \left(l_z \langle S_z \rangle_i M_{xy}^{\text{eff}} + l_y \langle S_y \rangle_i M_{xz}^{\text{eff}} + l_x \langle S_x \rangle_i M_{yz}^{\text{eff}} \right) \sin\theta \, d\theta \, d\phi \quad (1.9)$$

As illustrated in Figure 1.10b, transitions with different polarizations show different saturation magnetization behavior even though they have the same ground state. Therefore, provided the ground-state parameters of Equation 1.8 are known from EPR (which is generally the case for Kramers ions), VTVH MCD can be used to obtain the polarizations of the electronic transitions in a randomly oriented frozen solution of a transition metal complex, which aids in spectral assignment and provides fundamental insight.

Non-Kramers Ions: High-Spin Fe(II) S = 2   Non-Kramers ions have a very different ZFS behavior.[29] For a $S = 2$ ground state with a rhombic ligand field (Figure 1.11, where $E \neq 0$), ZFS can eliminate all the M_S degeneracy even in the absence of a magnetic field.

Thus, for the non-Kramers ion, the $\pm M_S$ doublets split and this typically leads to the lack of an EPR signal for integer spin systems as this splitting is generally greater than the microwave energy (X-band, 0.3 cm^{-1}), making integer spin systems difficult to probe experimentally. However, these splittings have a very dramatic effect on the
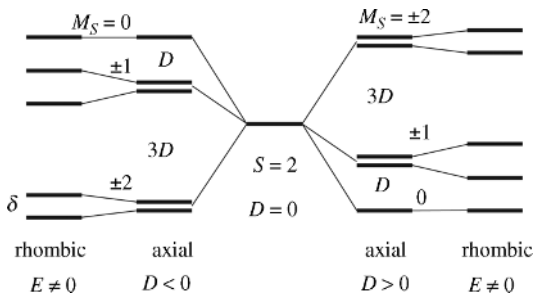
FIGURE 1.11   The effects of ZFS on a $S = 2$, non-Kramers ion.
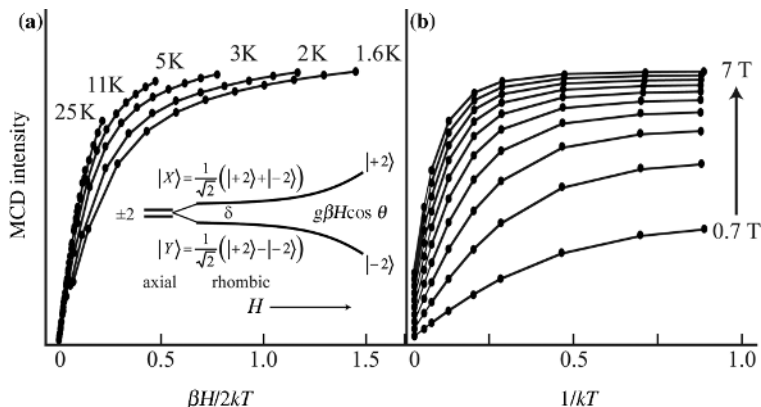
FIGURE 1.12   VTVH MCD for a non-Kramers $S=2$ system with rhombic distortion. Panel (a) plots the data as a function of $\beta H/2kT$ and panel (b) as a function of $1/kT$. The inset shows the effect of ZFS and a magnetic field on the $M_S=\pm 2$ ground-state wavefunction.[30]

VTVH MCD data for non-Kramers ions allowing the measurement of spin Hamiltonian parameters of EPR inactive centers.[29,34]

As shown in Figure 1.12a, a non-Kramers $S=2$ system with rhombic distortion will show significant nesting in its saturation magnetization curves.

Insight into the origin of this nesting can be obtained by replotting these data in a manner that uncouples the temperature and magnetic field dependencies of the MCD signal. This is plotted in Figure 1.12b for a series of fields, each with decreasing temperature to the right. At a given field, the system saturates at low temperatures, corresponding to population of only the lowest component of the ground state. However, the amplitude of the temperature-saturated MCD signal increases with increasing magnetic field (arrow in Figure 1.12a) requiring that the wavefunction of the lowest energy component of the ground state ($|Y\rangle$ in the inset of Figure 1.12) changes with magnetic field. This is exactly the behavior of a non-Kramers doublet depicted in the inset of Figure 1.12a. As indicated in the inset, in addition to the rhombic splitting of the non-Kramers doublet by δ, the wavefunctions are completely mixed at zero magnetic field ($|X\rangle = \frac{1}{\sqrt{2}}|+2\rangle + |-2\rangle$ and $|Y\rangle = \frac{1}{\sqrt{2}}|+2\rangle - |-2\rangle$). Increasing the field, Zeeman both splits the doublets (by $g\beta H \cos\theta$), where θ is the angle of the magnetic field relative to the molecular z-axis, and changes the wavefunctions such that the wavefunction of the lowest level goes from $\frac{1}{\sqrt{2}}(|2\rangle - |-2\rangle)$ at zero field, which is MCD inactive, to the pure $|-2\rangle$, which will have a large MCD signal based on its spin expectation value.

Equation 1.10 describes this non-Kramers doublet behavior and its fit to the VTVH MCD data in Figure 1.12a (with orientation averaging for a frozen solution) allows the spin Hamiltonian parameters to be obtained.[29,30] These, in turn, can be related to the ligand field splittings of the t_{2g} set of d-orbitals, as described in Ref. 7, which probe the π-interactions of the Fe(II)

with its ligand environment.

$$\Delta\varepsilon = A_{sat} \int_0^{\pi/2} \frac{\cos^2\theta \sin\theta}{\sqrt{\delta^2 + (g_{\parallel}\beta H \cos\theta)^2}} g_{\parallel}\beta H \times \tanh\frac{\sqrt{\delta^2 + (g_{\parallel}\beta H \cos\theta)^2}}{2kt} d\theta$$

$$(1.10)$$

Thus, for non-Kramers ions, VTVH MCD uses an excited state to obtain ground-state EPR parameters of EPR inactive, but paramagnetic, metal sites.

1.3   CHARGE TRANSFER EXCITED STATES

Ligands generally form σ-donor bonds with metal ion sites. Several common ligands in bioinorganic chemistry also have strong π-donor interactions with the metal (thiolates and phenolates, in particular).

As shown in Figure 1.13a, donor bonding interactions involve filled ligand valence orbitals at deeper binding energy relative to the metal d-orbitals. Donor bonding leads to ligand to metal charge transfer transitions that involve excitation of an electron from filled ligand valence orbitals to half-occupied and unoccupied metal d-orbitals. Ligands with intramolecular π-bonding in inorganic and organometallic chemistry also have low-lying unoccupied π^* orbitals that can have π-acceptor interactions with the occupied metal dπ orbitals (the d-orbitals available for π-overlap with the ligands) (Figure 1.13b). This π-backbonding often results in MLCT bands in the absorption spectrum. Here we focus on donor bonding, but both types of CT processes can result in a large change in electron density along the L−M bond leading to large electric dipole transition moments and intense absorption features polarized along the L−M bond (in contrast to their relatively weak contributions to the CD and MCD spectra, as discussed in Section 1.2). As developed below, the energies and intensities of CT transitions reflect the M−L bonding and can be used to quantitate the relative donor strength of the ligand. We first consider the simplest case of a one-hole Cu(II) complex and then the most complex case of a high-spin Fe(III) d^5 site.
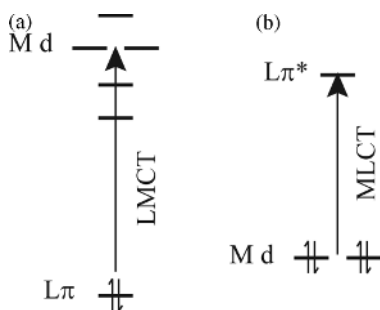
FIGURE 1.13   Schematic energy-level diagram depicting ligand to LMCT and MLCT transitions.
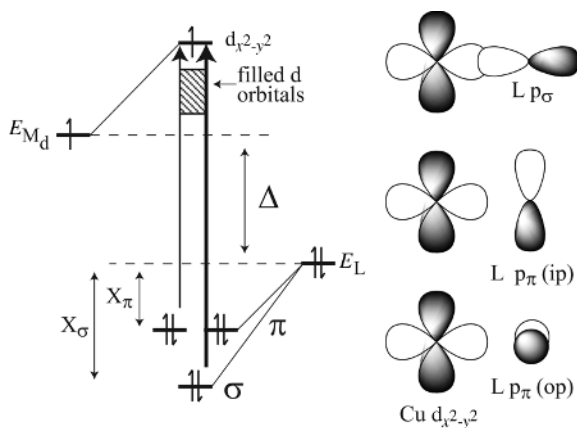
FIGURE 1.14 Orbital interactions (right in the x–y plane; ip = in plane and op = out of plane) and relevant MO diagram for a tetragonal Cu(II) complex.[7] Arrows represent the LMCT transitions with the relative intensity indicated by the width of the arrow.

1.3.1   Cu(II) Charge Transfer Transitions

As developed above, Cu(II) complexes generally have tetragonal geometries due to the Jahn–Teller effect with strong donor bonding in the equatorial plane. This leads to a half-occupied $d_{x^2-y^2}$ valence orbital with lobes oriented along the L−M bonds due to the strong antibonding interactions with the ligands.

Figure 1.14 shows the orbital interactions and a relevant molecular orbital (MO) diagram for this case. In Figure 1.14, we focus on monoatomic ligands that have three valence p-orbitals available for bonding with the metal ion, and first consider the energies of the CT transitions. E_L is the ligand valance ionization energy. As the ligand becomes less electronegative (i.e., easier to oxidize), LMCT transitions shift down in energy (e.g., CuF_4^{2-} ($>41{,}500\,cm^{-1}$) $> CuCl_4^{2-}$ ($22{,}500\,cm^{-1}$) $> CuBr_4^{2-}$ ($16{,}500\,cm^{-1}$)).[35,36] E_M is the metal valence ionization energy that depends on the effective nuclear charge on the metal ion (Z_{eff}). This is determined by the atomic number (Z) of the metal ion, its oxidation state, and the number and types of donor ligands. From the MO diagram in Figure 1.14, ligand valence orbitals are stabilized and metal orbitals destabilized by forming ligand–metal bonds. This is described by Equation 1.11, where $E_L - E_M = \Delta$ is the energy gap of the M and L valence orbitals before bonding, and $\int \phi_M \mathcal{H} \phi_L \, d\tau$ is the resonance integral of the molecular Hamiltonian that is proportional to the overlap of the metal and ligand orbitals ($S_{ML} = \int \phi_M \phi_L \, d\tau$) that results in bond formation.[37]

$$X = \frac{-\left(\int \phi_M \mathcal{H} \phi_L \, d\tau\right)^2}{E_L - E_M} \tag{1.11}$$

As shown in Figure 1.14, the three valence p-orbitals of a monoatomic ligand split into two sets upon bonding to the metal. The p_z (in a local coordinate system with each ligand's z-axis directed along the L−M bond) orbital is oriented along the M−L bond and has σ-overlap with the metal d-orbitals. The p_x, p_y set are perpendicular to the M−L bond and available for π-overlap resulting in the in-plane and out-of-plane π-interactions shown in Figure 1.14. Since σ-overlap is greater than π-overlap, $X_{p\sigma} > X_{p\pi}$ and results in a doubly degenerate ligand $p_\pi \rightarrow \mathrm{Cu}(d_{x^2-y^2})$ CT at lower energy than the ligand $p_\sigma \rightarrow \mathrm{Cu}(d_{x^2-y^2})$ CT.

The CT intensities also reflect orbital overlap. In the limit of low overlap, the electric dipole transition moment integral is given by $\int \psi_g \vec{r} \psi_e \, d\tau \approx r S_{M'L}$, where r is the M−L bond length and $S_{M'L}$ is the overlap integral for the ligand donor (L) and metal acceptor orbitals (M′) involved in the CT process.[38] From Figure 1.14, it can be seen that p_σ has significant overlap with the metal $d_{x^2-y^2}$ orbital producing an intense ligand $p_\sigma \rightarrow \mathrm{Cu}\, d_{x^2-y^2}$ CT transition at high energy. The p_π set has no overlap with the $d_{x^2-y^2}$ orbital resulting in a doubly degenerate lower energy weak π CT (its limited intensity deriving from configuration interaction with the σ CT).[39] In summary, for Cu (II) complexes, the orbitals involved in the L−M bonds result in a lower energy weak π and a higher energy intense σ to Cu CT transition. This pattern can change for polaatomic ligands where intraligand bonding dominates and effects the valence orbitals of the ligand available for bonding to the metal.

Proceeding further, the CT intensity can be used to quantitate the donor strength of a ligand.[40] The donor strength is given by the amount of metal character in the ligand valence orbital due to bonding, and reciprocally the amount of ligand character mixed into the metal d-orbital. From Equation 12a, c^2 quantitates the amount of electron density donated by the occupied ligand valence orbital to the metal through bonding.

$$\psi_M^* = \sqrt{1-c^2}(\phi_M) - c(\phi_L)$$
$$\psi_L^* = \sqrt{1-c^2}(\phi_L) + c(\phi_M)$$

(1.12a)

$$\int \psi_g \vec{r} \psi_e \, d\tau = c\sqrt{1-c^2} \int \phi_M \vec{r} \phi_M \, d\tau + (1-c^2) \int \phi_L \vec{r} \phi_M \, d\tau$$
$$- c^2 \int \phi_M \vec{r} \phi_L \, d\tau - c\sqrt{1-c^2} \int \phi_L \vec{r} \phi_L \, d\tau$$

(1.12b)

Substitution of the wavefunctions in Equation 12a into the electron dipole transition moment expression generates Equation 12b. In Equation 12b, the first term on the right-hand side describes a d → d transition that will not contribute to the intensity and from calculations the last term is dominant.[41] This is the ligand–ligand term, which in the dipole approximation reflects the overlap of the ligand character in the bonding (donor) and antibonding (acceptor) molecular orbitals involved in the electronic transition. For this to be nonzero, the ligand character in the donor and acceptor orbitals has to be the same, which then gives Equation 1.13, where $\vec{r}$ is

aligned along the L−M bond.

$$c\sqrt{1-c^2}\int\phi_L\bar{r}\phi_L\,d\tau \cong c\bar{r} \tag{1.13}$$

Since CT intensity goes as the square of the transition moment integral, this shows that CT intensity is proportional to c^2, the ligand donor strength. From molecular orbital theory, $c \approx -\left(\int\phi_M H\phi_L d\tau\right)/(E_L-E_M)$ and is therefore proportional to the L−M overlap as described above. Also, c^2 and therefore CT intensity increases as $E_L - E_M$ decreases. This leads to the very important concept that *low-energy, intense CT reflects highly covalent L−M bonds (i.e., strong donors)*. This high covalency can play a major role in activating a metal center for reactivity.

1.3.2 High-Spin Fe(III) Charge Transfer Transitions

High-spin Fe(III) centers have five half-occupied d-orbitals (α spin) that are available for bonding. Since the transition energy decreases with increasing metal Z_{eff}, high-spin Fe(III) complexes often exhibit low-energy LMCT transitions. From the Tanabe–Sugano diagram (Figure 1.4, left), the high-spin Fe(III) ground state is $^6A_{1g}$, therefore lacking a Jahn–Teller distortion, and the strong z-axis for quantization of the d-orbitals is usually determined by the most covalent L−M bond. This should also contribute the dominant LMCT transitions to the absorption spectrum.

From Figure 1.15, the ligand p_z orbital will have strong σ-overlap with the metal d_{z^2} producing a high-energy intense CT, while the ligand $p_{x,y}$ orbitals have π-overlap with the d_{xz}/d_{yz} orbitals resulting in lower energy weaker π CT. Note that the hole produced in the ligand valence orbital will couple with the unpaired electrons on the metal and give a number of many-electron states; however, electron–electron repulsion is small between the metal and ligand centers. The LMCT transitions produce d^{n+1} final states given by the appropriate Tanabe–Sugano diagram, but with ligand field parameters reflecting the now reduced, in this case Fe(II), metal center.[42]
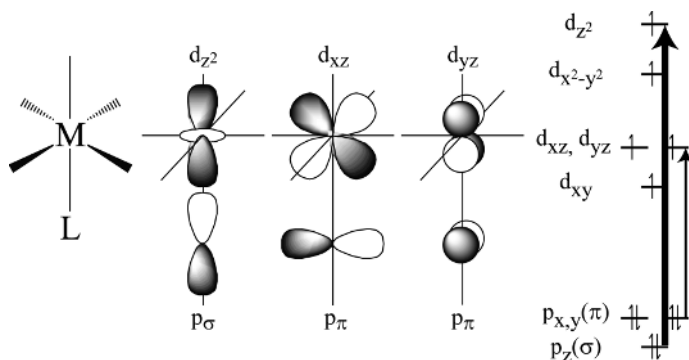

FIGURE 1.15 Metal ligand overlap and MO diagram for a O_h high-spin Fe(III) complex. Arrows indicate the LMCT transitions. The bold arrow shows the more intense σ CT

Thus, while Cu(II) CT transitions reflect σ-bonding, in Fe(III) sites these can quantitate both σ- and π-bonding interactions of the ligand with the metal d-orbitals. Identification of the specific ligand orbital in the CT process is accomplished by a combination of resonance Raman and polarized absorption spectroscopies (the CT transition being polarized along the L−M bond). The latter can be accomplished either in a single crystal using polarized light or in frozen solution using VTVH MCD, as described in Section 1.2.3.2.

1.4   CORE EXCITED STATES: X-RAY ABSORPTION SPECTROSCOPIES

The complete electronic energy level diagram of a representative transition metal complex (D_{4h} $CuCl_4^{2-}$) is given in Figure 1.16.

In Sections 1.2 and 1.3, we focused on transitions between valence orbitals spanning a range of ~5 eV (~40,000 cm^{-1}). Here we consider excitations of core
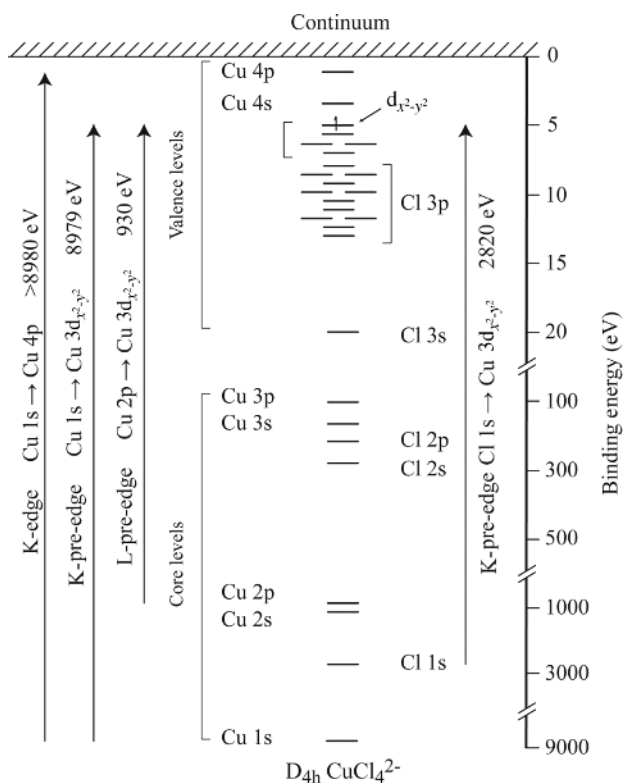
FIGURE 1.16   The complete electronic energy level diagram of D_{4h} $CuCl_4^{2-}$ depicting the various XAS pre-edge and edge transitions.[17]
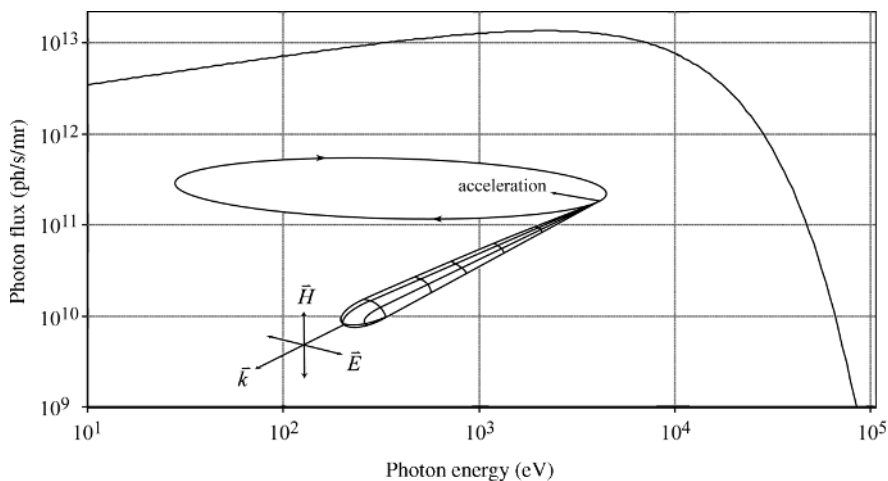
FIGURE 1.17 Photon flux versus energy for the SPEAR3 bending magnet spectrum at the Stanford Synchrotron Radiation Lightsource, Stanford University, SLAC.

electrons into unoccupied and half-occupied valence orbitals. Metal 1s excitation corresponds to the metal K-edge (for Cu this is at ~9000 eV), ligand 1s excitation generates the ligand K-edge (for Cl at ~2820 eV), and metal 2p excitation generates the metal L-edge (for Cu(II) at ~930 eV) (Figure 1.16). Absorption spectra taken at these X-ray energies require synchrotron radiation. This is produced by electrons moving in ultrahigh vacuum ($<10^{-7}$ Torr) at relativistic velocities in a storage ring with paths bent by a magnetic field.

As shown in Figure 1.17, the emitted synchrotron radiation is continuous in the X-ray region (in contrast to the discrete energies of X-ray anodes), intense and polarized in the plane of the electron's orbit (inset).

A representative XAS spectrum (metal K-edge) is generally divided into four regions, as indicated in Figure 1.18.

The extended X-ray absorption fine structure region starts at ~50 eV above the edge and corresponds to an electron excited from the core into the continuum in Figure 1.16.[5] Scattering of the electron from adjacent ligands leads to constructive and destructive interferences with the outgoing de Broglie wave depending on the electron kinetic energy. The Fourier transform of this provides structure-sensitive information on the metal site in solution. To lower energy of the EXAFS is the near-edge region, whose information content is currently being developed through multiple scattering theory.[43] The structure in the near-edge region corresponds to shape resonances where the ionized electron is trapped by the potential of the coordination environment. This can provide structural insight complementary to EXAFS.[44] Here we focus on the edge and pre-edge regions that are rich in electronic structural information and systematically develop their information content.
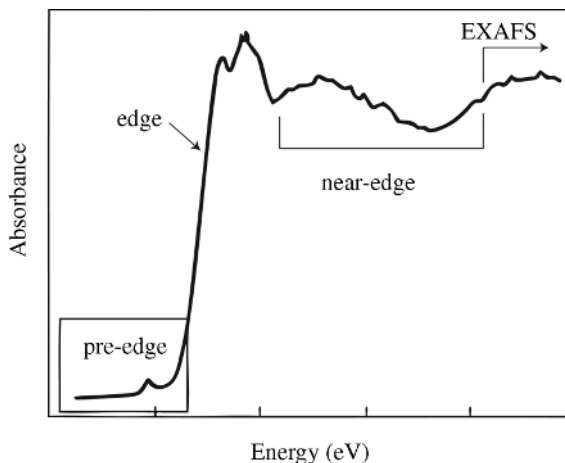
FIGURE 1.18   Representative metal K-edge XAS spectrum.

1.4.1   Metal K-Edges

1.4.1.1   Cu(I) d¹⁰   It is instructive to first consider a reduced Cu site that has a filled subshell d^{10} electron configuration. This cannot be studied by most of the spectroscopic methods used in inorganic and bioinorganic chemistry (the alternative approach is photoelectron spectroscopy (PES) that is presented in Ref. 45). The edge for a Cu(I) complex is at ~8990 eV and corresponds to the threshold energy for
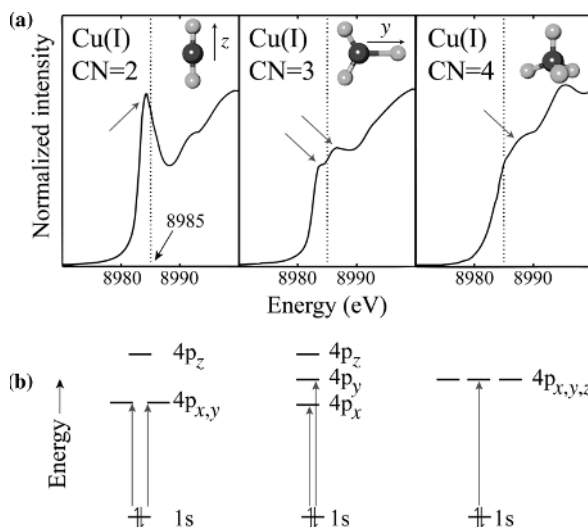

FIGURE 1.19   (a) Pre-edges for various coordination geometries of Cu(I) complexes.[47] (b) MO diagrams giving rise to the pre-edge features.

ionization of a metal core 1s electron into the continuum in Figure 1.16. As with PES, the edge energy depends on the effective nuclear charge of the metal ion and is referred to as the chemical shift of the core level.[46] Z_{eff} is defined by the oxidation state of the metal, its coordination number, and the strength of the donor interaction of the ligands with the metal ion (i.e., covalency). For Cu(I), all the d-orbitals are filled and the pre-edge feature corresponds to a Cu 1s $\rightarrow$ 4p transition, which, as shown in Figure 1.19, occurs at $\sim$8984 eV.

This transition is g $\rightarrow$ u with $\Delta L = +1$ and is therefore electric dipole allowed and intense in XAS. The energy and shape of this feature strongly depend on the ligand field of the Cu(I) site through its effect on the Cu 4p orbitals (Figure 1.19b).[47] For a two-coordinate linear Cu(I) site (left of Figure 1.19), the $4p_z$-orbital is destabilized due to antibonding interactions with the ligands leading to a low-energy, intense, sharp pre-edge feature at 8984 eV corresponding to the 1s $\rightarrow$ $4p_{x,y}$ transitions (arrows in Figure 1.19). For three-coordinate Cu(I), interaction with the third ligand in the now equatorial plane (y–z plane) removes the degeneracy of the $4p_{x,y}$ producing a doublet pattern in the 8984 eV peak (arrows in the center of Figure 1.19). Finally, for four-coordinate Cu(I), all 4p orbitals are involved in equivalent repulsive interactions with the ligands and no pre-edge intensity is present in the Cu K-edge below 8985 eV.

1.4.1.2   Cu(II) d^9   Cupric complexes typically have a hole in the $d_{x^2-y^2}$ orbital (Figure 1.5b and c) allowing a 1s $\rightarrow$ 3d transition, which occurs below the edge at $\sim$8979 eV. The s $\rightarrow$ d transition is electric dipole forbidden (g $\rightarrow$ g and $\Delta l = 2$); therefore, the transition will be very weak, but is observed even in centrosymmetric complexes (i.e., those with inversion symmetry) as shown in the blowup of the pre-edge region in Figure 1.20 for the D_{4h} $CuCl_4^{2-}$ complex.

The origin of the nonzero intensity for this transition was determined by polarized single-crystal XAS at the Cu K-edge.[48] As shown in Figure 1.20a, light was propagated into the $CuCl_4^{2-}$ crystal with its $\vec{E}$ vector oriented in the molecular xy-plane and the complex was rotated around the z-axis (by an angle ϕ). The spectra in Figure 1.20 show that the intensity of the 8979 eV peak varies with ϕ. The intensity of the pre-edge peak plotted as a function of ϕ (inset of Figure 1.20) shows that it maximizes every 90°, when the $\vec{E}$ and $\vec{k}$ vectors bisect the L$-$M bonds. This demonstrates that the intensity derives from an electric quadruple mechanism, where $\hat{M}_{(electric\ quadrupole)}$ in Equation 1.2 is given by Equation 1.14, indicating that the $\vec{E}$ and $\vec{k}$ vectors of light project out the x and y components of the electron's momentum (p) and position (r).

$$I \propto \left\langle 1s \left| \left(\vec{E} \cdot \vec{p} \right) \left(\vec{k} \cdot \vec{r} \right) \right| \Psi_e \right\rangle \qquad (1.14)$$

The quadrupole operator transforms as M_{xy} and makes the 1s $\rightarrow$ 3d transition electric quadrupole allowed when the $d_{x^2-y^2}$ orbital (in molecular coordinates) bisects the $\vec{k}$ and $\vec{E}$ vectors (which define the laboratory coordinates). Quadrupole intensity is usually very low; however, at $\sim$9000 eV the wavelength of light is $\sim$1.4 Å and in this case the long-wave approximation no longer holds and higher terms in the multipole expansion in Equation 1.2 become important.
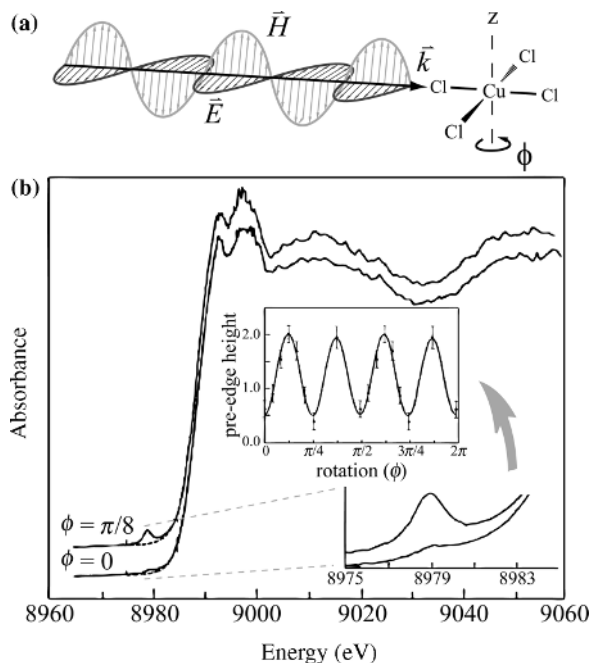
FIGURE 1.20   XAS spectra of D_{4h} $CuCl_4^{2-}$.[48] Panel (a) shows the orientation of the X-ray beam with the complex and the angle (ϕ) by which the complex was rotated. Insets show a blowup of the pre-edge region and a plot of the pre-edge intensity as a function of ϕ.

In going to complexes lacking a center of inversion (i.e., noncentrosymmetric), the $d_{x^2-y^2}$ orbital can mix with the 4p-orbitals of the metal. From the above discussion, the 1s $\rightarrow$ 4p transition is electric dipole allowed. In the X-ray region, electric dipole intensity is ~100-fold higher than electric quadrupole intensity; thus, a few percent of 4p mixing into a d-orbital can have a large effect on the pre-edge intensity.

This is developed in Figure 1.21 for the blue copper site in plastocyanin where the issue of Cu 4p mixing into the $d_{x^2-y^2}$ orbital was critical to understanding the unique EPR properties of the active site.[49] From the orientational averaged XAS spectrum in Figure 1.21a, the 8979 eV pre-edge peak in blue copper is much more intense than the 8979 eV peak in D_{4h} $CuCl_4^{2-}$ reflecting the 4p mixing in the noncentrosymmetric protein active site. Importantly, from the polarized spectra of blue copper in Figure 1.21, the intensity is high only when the site was oriented such that the $\vec{E}$ vector of light is in the xy-plane showing that $4p_{x,y}$ is mixed into the $d_{x^2-y^2}$ ground-state wavefunction of the blue copper site. These pre-edge data eliminated a $4p_z$ mixing model that had generally been invoked to explain for the small Cu hyperfine coupling and allowed focus on the now accepted model that the small $A_{\|}$ value of the blue copper site actually reflects its high covalent delocalization into a thiolate ligand that activates the site for its function of rapid, directional electron transfer.[50]
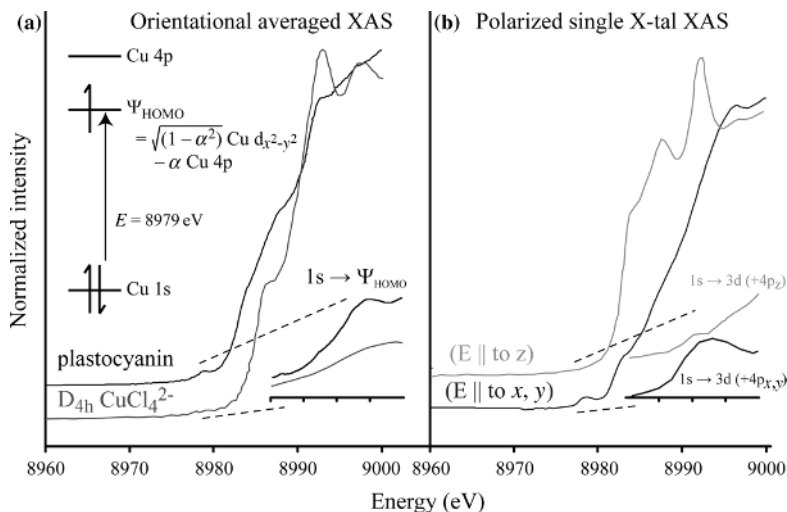
FIGURE 1.21 XAS spectra of the blue copper site in plastocyanin and the D_{4h} $CuCl_4^{2-}$ complex.[49] Panel (a) shows the orientational averaged spectra with a blowup of the pre-edge region and the inset shows an energy diagram showing the edge transition. Panel (b) shows the polarized single crystal (X-tal) spectra with the $\vec{E}$ vector of light oriented in the directions indicated. Note that with $\vec{E}$ parallel to the z-axis no pre-edge feature is observed (this is the direction for $4p_z$ mixing).

In summary, the intensity of a metal K-pre-edge peak is low and dominantly reflects a distortion of the metal site from centrosymmetric that allows metal 4p mixing into the valence 3d orbitals.

1.4.1.3 Fe(III) d^5   In going to a high-spin Fe(III) center there are now five half-occupied valence d-orbitals available for 1s → 3d transitions, each having a quadrupole and a 4p electric dipole contribution; the latter if the site is noncentrosymmetric. These transitions split in energy into a number of d^{n+1} final states due to the ligand field splitting of the d-orbitals combined with electron–electron repulsions. The d^6 final states available from a high-spin d^5 ground state 1s core excitation are fairly straightforward. The d^6 free ion has a ^5D high-spin state that splits into $^5T_{2g}$ and ^5E_g states separated by 10Dq for an O_h site.

As shown in Figure 1.22a, for a six-coordinate center, even in a protein, the intensity of the pre-edge (at ~7112 eV for Fe(III)) is low and has dominantly quadrupole character.[51] Here we see two peaks in a 3:2 intensity ratio split by the 10Dq of the O_h ligand field. In going to a four-coordinate, T_d structure (Figure 1.22b) 10Dq decreases, as 10Dq (T_d) = –4/9 10Dq (O_h) and the intensity of the peak greatly increases. The latter derives from the fact that the 4p orbitals have t_2 symmetry in T_d and will mix with the 3d set having the same symmetry resulting in significant electric dipole character in the higher energy (1s → 3d (t_2)) pre-edge transition. In going to a five-coordinate, square pyramidal (C_{4v}) symmetry, the $4p_z$ now mixes into
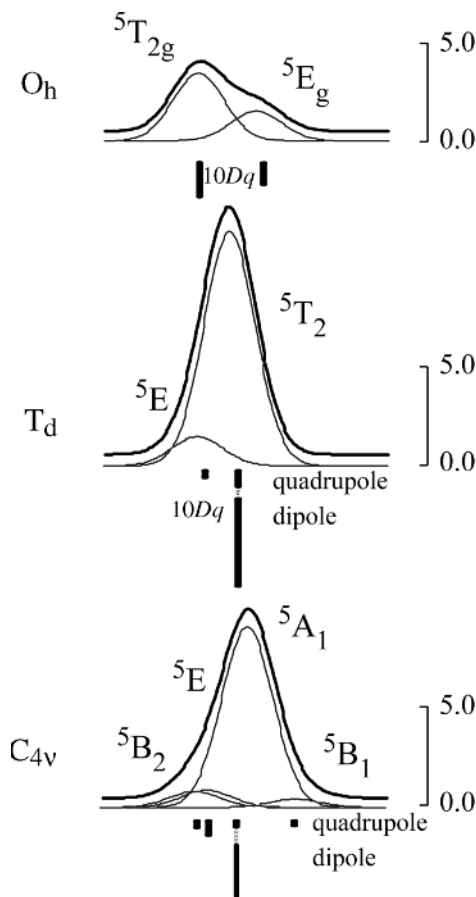
FIGURE 1.22   Effect of site geometry on the pre-edge of Fe(III) complexes.[51] Below each spectrum the bar graphs indicate the contribution to the intensity from electric dipole and quadrupole mechanisms for each final state.

the d_{z^2}-orbital that is energy shifted due to the strength of the axial interaction with the Fe(III) (Figure 1.22c). Thus, for high-spin Fe(III), the pre-edge feature is more intense in five- and four-coordinate sites and the intensity/energy distribution reflects the specific ligand field mixing of 4p character into the d^{n+1} final states.[51]
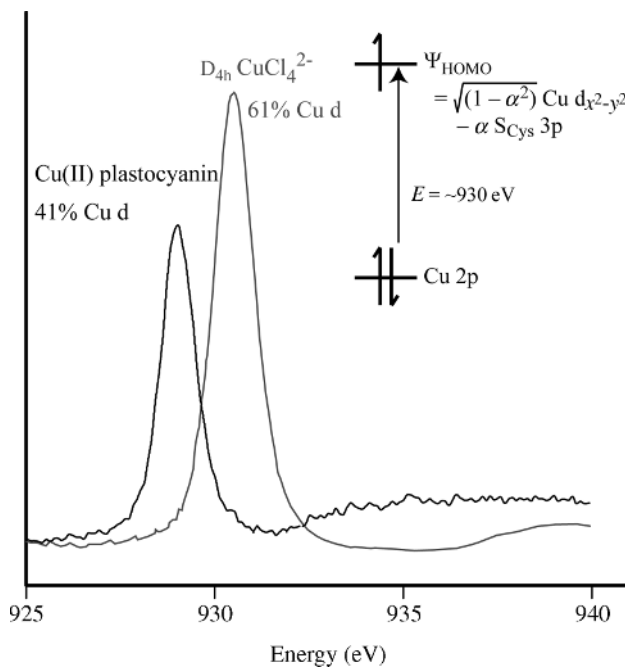
1.4.2   Metal L-Edges

Metal L-edge XAS mostly focuses on transitions from the $2p^6$ core. The $2p \rightarrow 3d$ and $2p \rightarrow 4s$ are electric dipole allowed with the $p \rightarrow d$ channel being ~20-fold more intense.[52] Therefore, L-edges are a more direct method to study d valence levels relative to the metal K-edges. Also, the spectra are taken at much lower photon

energies; therefore, they have higher resolution ($\sim$0.3 eV relative to $\sim$1.0 eV for K-edges). However, the energy range of interest is $\sim$500 to 1000 eV and the experiment must be done under ultrahigh vacuum conditions. The $2p^5$ excited configuration gives a ^2P final state that has spin and orbital angular momenta that spin–orbit couple to produce the $^2P_{3/2}$ (L_3-edge) and $^2P_{1/2}$ (L_2-edge peaks), split by 10–20 eV depending on Z with the L_3 at lower energy with approximately twice the intensity.

1.4.2.1 Cu(II)

For d^9 Cu(II) complexes, L-edge XAS is fairly straightforward. There can only be one $2p^63d^9 \rightarrow 2p^53d^{10}$ transition, producing the L_3 feature of the pre-edge at $\sim$930 eV (inset of Figure 1.23) and L_2 feature at $\sim$20 eV higher energy.

Since $2p \rightarrow 3d$ is electric dipole allowed and the Cu 2p orbital is localized on the Cu nucleus, the intensity of the Cu L-edge is a direct probe of the Cu d character in the half-occupied molecular orbital of the complex (($1 - \alpha^2$), in the inset of Figure 1.23) giving the covalency of the Cu site. As the L-edge intensity decreases, the ligand character increases, reflecting a more covalent active site. This was an important result in Cu bioinorganic chemistry. As shown in Figure 1.23, the L_3-edge intensity of the Cu(II) blue copper site in plastocyanin is much lower than that of D_{4h} $CuCl_4^{2-}$. Thus, there is less metal character; that is, the blue copper site is more covalent.[53] Since

D_{4h} $CuCl_4^{2-}$
61% Cu d

Ψ_{HOMO}
$= \sqrt{(1-\alpha^2)}$ Cu $d_{x^2-y^2}$
$- \alpha$ S_{Cys} 3p

Cu(II) plastocyanin
41% Cu d

$E = \sim$930 eV

Cu 2p

Energy (eV)

FIGURE 1.23 L-edge XAS spectra of the blue copper site in plastocyanin and D_{4h} $CuCl_4^{2-}$.[53] Inset shows the relevant MO diagram and half-occupied HOMO wavefunction.

a variety of spectroscopies give for D_{4h} $CuCl_4^{2-}$ a ground state with 61% $d_{x^2-y^2}$ character, the intensity ratio in Figure 1.23 shows that the blue copper site is highly covalent with 41% Cu d character.[53] This provided an explanation for the small hyperfine coupling in the blue copper site mentioned above and is further probed by ligand K-edge XAS in Section 1.4.3.

1.4.2.2   Fe(III) d⁵

1.4.2.2   Fe(III) d^5   As for the K-edge, L-edges in d^5 Fe(III) sites have transitions to the fives holes in its d-orbitals. These are again energy split due to the ligand field but we must also include the large effects of electron–electron repulsion and spin–orbit coupling that dominate the L-edge spectral shape.[52] A multiplet calculation for the $2p^6 3d^n \rightarrow 2p^5 3d^{n+1}$ final states includes the ligand field splitting of d-orbitals, 3d–3d and 2p–3d electron–electron repulsion, and p and d spin–orbit couplings. For a high-spin Fe(III) complex, this produces many states indicated by the vertical lines below the spectra in Figure 1.24a. These are lifetime and instrument broadened to produce the L-edge spectral band shape shown.

Note in comparing Figure 1.24a and b that the shape strongly depends on the ligand field and greatly changes in going from high- to low-spin Fe(III) complexes. As for Cu L-edges, the total intensity decreases as the covalency increases and importantly for L-edges of metal sites with multiple holes, the differential orbital covalency (DOC) (the difference in the $t_2(\pi)$ and $e(\sigma)$ covalencies of the half-occupied and unoccupied d-orbitals) can greatly affect the band shape.[54] This can be seen in Figure 1.24c, which compares the L-edge spectra of a low-spin Fe(III) complex with only σ-donor ligands
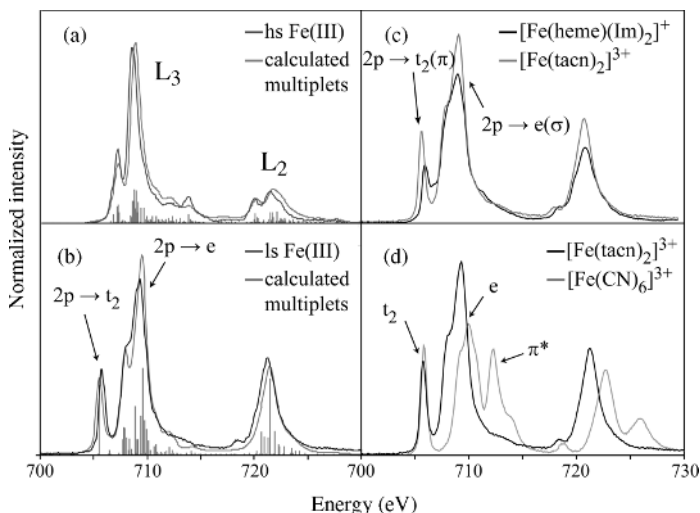

FIGURE 1.24   L-edge XAS spectra of Fe^{III} complexes: (a) high spin, (b) low spin,[54] (c) without (tacn) and with (heme) π-donor bonding, reflecting differential orbital covalency, and (d) without (tacn) and with (CN) π-backbonding.[56] The vertical lines in (a) and (b) represent the calculated final states that are broadened to give the resultant, superimposed calculated spectra.

to that of low-spin Fe(III) where there is now π-donor bonding as well. Note that the low-energy peak at 706 eV is dominantly a $2p \rightarrow 3d_{(t_{2g})}$ transition into the $d\pi$ set of orbitals, while the intense peak at ~710 eV reflects the multiplet split $2p \rightarrow 3d_{(e_g)}$ transitions to the $d\sigma$ set. The fact that the Fe(III) heme site has lower intensity in the t_2 hole experimentally quantitates that the tetrapyrole ligand is a very strong π-donor that governs the metal $d\pi$ character and plays a key role in the electron transfer reactivity of heme sites.[55] Finally, Figure 1.24d demonstrates that the L-edge is perhaps the most direct spectral method to quantitate π-backbonding (compared to a vibrational frequency that has contributions from σ-donor and mechanical coupling with other vibrations in addition to π-backbonding). Figure 1.24d shows that ferricyanide has a new intense feature at ~3 eV above the $2p \rightarrow 3d\sigma$ peak.[56] This involves Fe 2p transitions into the CN π^* orbitals that gain d character, hence L-edge intensity due to their π-acceptor interactions with the occupied d-orbitals on the Fe. The details of using the L-edge to experimentally quantitate backbonding are presented in Ref 56.

1.4.3 Ligand K-Edges

The ligand K-pre-edge corresponds to the ligand $1s \rightarrow$ metal 3d transition (Figure 1.25).
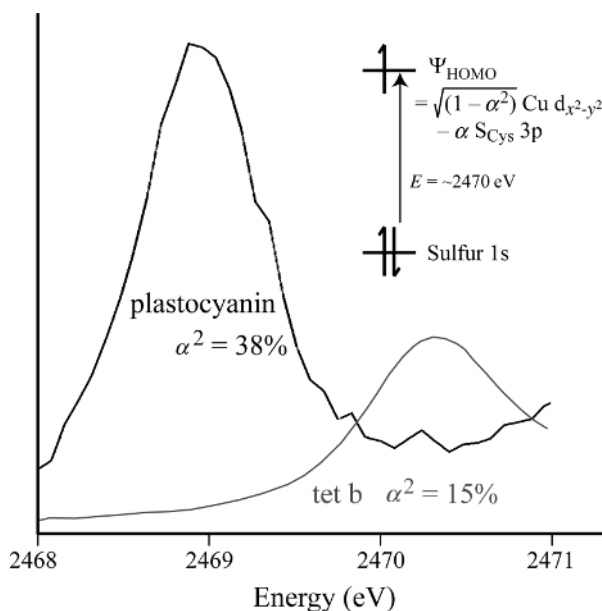
FIGURE 1.25 Sulfur K-edge spectra for blue copper site in plastocyanin and the Cu(II) model complex tet b.[49] Inset shows the MO diagram for a transition to the half-occupied HOMO.

This method has been applied to second (N and O) and third (S and Cl) row coordinating atoms.[6] We focus on sulfur here as the covalency of S−M bonds has played an important role in bioinorganic chemistry and S K-edge spectroscopy has provided the most direct method to quantitate these bonds. The S K-pre-edge is at 2470 eV and involves the L 1s → M 3d transition. Since the 1s orbital is localized on the sulfur nucleus and s → p is electric dipole allowed, the S K-pre-edge intensity directly reflects the S 3p character mixed into the M 3d orbitals. Thus, S K-edge intensity provides a direct probe of the covalency of a sulfur–metal bond. This can be compared to the ligand superhyperfine coupling in EPR (Chapter 3) but is appropriate for unoccupied as well as half-occupied valence orbitals and the site does not have to be EPR active.

1.4.3.1 *Cu(II) d^9*
The blue copper active site in plastocyanin is used as an example of S K-edge spectroscopy as this method was first applied to this site.[49] When reduced, the blue copper site has no sulfur K pre-edge feature. However when oxidized, the blue copper site exhibits an intense absorption peak at 2470 eV (Figure 1.25). This peak is 2.5-fold more intense than the S pre-edge feature of a model complex (tet b) that has a fairly normal thiolate S−Cu(II) bond with 15% covalency. The intensity ratio in Figure 1.25 demonstrates that $\alpha^2 = 38\%$ in the half-occupied $d_{x^2-y^2}$ molecular orbital of blue copper (inset of Figure 1.25). This high covalency couples the Cu center into specific superexchange pathways through the protein and activates it for long-range electron transfer in biology.[50]

1.4.3.2 *High-Spin Fe(III)*
Again, for high-spin Fe(III) there can be 1s → 3d transitions to five half-occupied molecular orbitals. These produce d^{n+1} multiplet final states split in energy by electron–electron repulsion and the ligand field splitting of the d-orbitals.

In addition, as illustrated in Figure 1.26 for a T_d d^5 ion as found in the iron–sulfur proteins, the $d\pi(e)$ and $d\sigma(t_2)$ orbitals will have differences in covalency (i.e.,
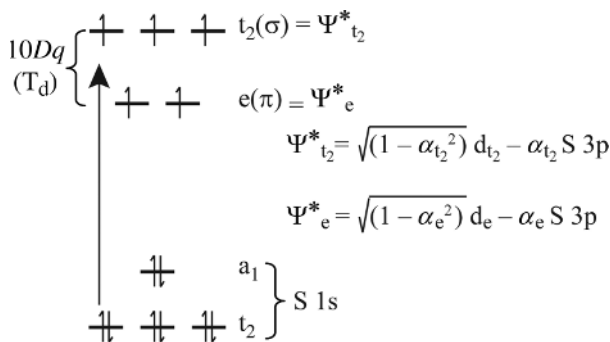
FIGURE 1.26   MO diagram for a high-spin d^5 ion in a T_d ligand field with sulfur ligands. Right-hand side gives the wavefunctions.
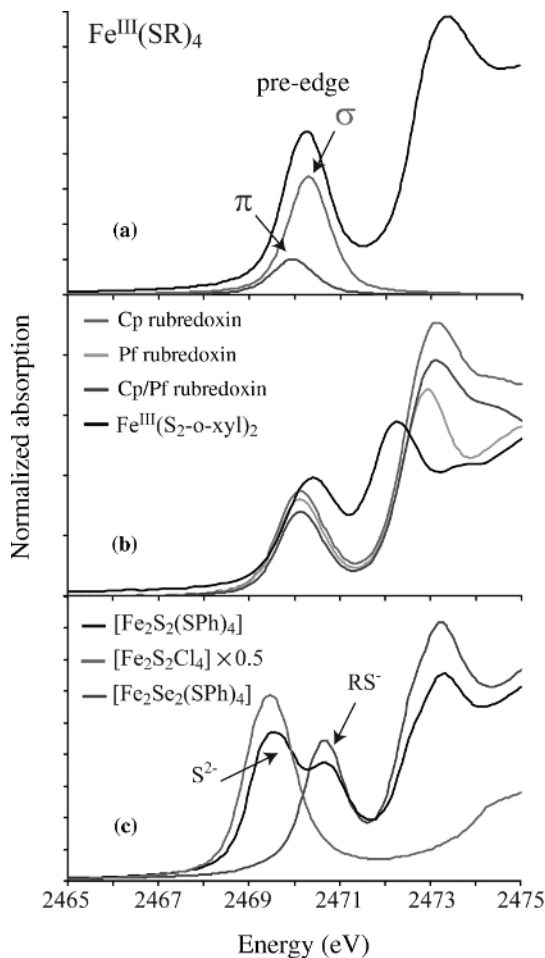
FIGURE 1.27   Sulfur K-pre-edge XAS[59] for (a) $Fe^{III}(SR)_4^-$ model complex, (b) the model compared to several rubredoxins to illustrate the effect of the protein environment in reducing covalency, and (c) Fe_2S_2-type complexes with RS_4 (black) replaced by Cl^- (red) or μS^{2-} by μSe^{2-} (blue). (See the color version of this figure in Color Plates section.)

S character, therefore S pre-edge intensity) distributed over the d^{n+1} final states. In Figure 1.27a for a high-spin $Fe(III)(SR)_4^{1-}$ complex, the thiolate pre-edge is well separated from the S-edge and two overlapping peaks are observed.[57]

   These correspond to the S $1s \rightarrow M\, d\pi(e)$ and S $1s \rightarrow M\, d\sigma(t_2)$ transitions split in energy by $10Dq$ (in the d^6 final state). The resolved intensities provide the π and σ covalencies (i.e., thiolate S character) in the d-orbitals of this site. In a comparison of the S K-edge data for the iron–sulfur model complexes of Holm and collaborators[58] to the proteins with structurally congruent sites, the intensity is generally decreased

(Figure 1.27b[57]). This reflects the electrostatic effects of H-bonding to the sulfur that reduces their donor interactions to the iron. This destabilizes the oxidized more than the reduced state and can make a major contribution to tuning up the reduction potentials of iron–sulfur proteins. Finally, the pre-edge energy depends on the Z_{eff} of the sulfur ligand that produces a chemical shift of the core 1s orbitals. As shown in Figure 1.27c, the Z_{eff} of bridging sulfide is very different from that of thiolate allowing pre-edge transitions from these chemically different ligands to be resolved for the same active site and their individual contributions to bonding quantified.[59] This has proved very important in understanding why $[Fe_2S_2]^+$ mixed valent sites are localized while $[Fe_4S_4]^{2+}$ clusters are delocalized even in low-symmetry protein environments.[60]

1.5   CONCLUDING COMMENTS

In this chapter, we have developed the information content of different excited state spectroscopic methods in terms of ligand field theory and the covalency of L−M bonds. Combined with the ground-state methods presented in the following chapters, spectroscopy and magnetism experimentally define the electronic structure of transition metal sites. Calculations supported by these data can provide fundamental insight into the physical properties of inorganic materials and their reactivities in catalysis and electron transfer. The contribution of electronic structure to function has been developed in Ref. 61.

ACKNOWLEDGMENTS

REFERENCES

1. Solomon, E. I.; Lever, A. B. P. *Inorganic Electronic Structure and Spectroscopy Methodology;* Wiley: New York; Vol. 1, 1999.

2. Solomon, E. I.; Lever, A. B. P. *Inorganic Electronic Structure and Spectroscopy Applications and Case Studies*; Wiley: New York; Vol. 2, 1999.

3. Ballhausen C. J. *Introduction to Ligand Field Theory*; McGraw-Hill: New York, 1962.

4. Lever A. B. P. *Inorganic Electronic Spectroscopy*; 2nd edition, Elsevier Science Publishers: Amsterdam, 1984.

5. Zhang H. H.; Hedman B.; Hodgson K. O. In *Inorganic Electronic Structure and Spectroscopy*; Solomon E. I.; Lever A. B. P., Eds.; Wiley: New York, 1999; Vol. 1, p 513.

6. Solomon E. I.; Hedman B.; Hodgson K. O.; Dey A.; Szilagyi R. K. *Coord. Chem. Rev.* **2005**, *249*, 97.

7. Solomon E. I.; Hanson M. A. In *Inorganic Electronic Structure and Spectroscopy*; Solomon E. I.; Lever A. B. P., Eds.; Wiley: New York, 1999; Vol. 2, p 1.

8. Colman P. M.; Freeman H. C.; Guss J. M.; Murata M.; Norris V. A.; Ramshaw J. A.; Venkatappa M. P. *Nature* **1978**, *272*, 1978.

9. Solomon E. I.; Lowery M. D. *Science* **1993**, *259*, 1575.

10. Szilagyi R. K.; Metz M.; Solomon E. I. *J. Phys. Chem. A* **2002**, *106*, 2994.

11. Davydov A. S. *Quantum Mechanics*; NEO Press: Ann Arbor, 1966.

12. Sugano S.; Tanabe Y.; Kamimura H. *Multiplets of Transition-Metal Ions in Crystals*; Academic Press: New York, 1970.

13. Bethe H. *Ann. Phys.* **1929**, *395*, 133.

14. Racah G. *Phys. Rev.* **1942**, *62*, 438.

15. Jørgensen C. K. *Absorption Spectra and Chemical Bonding Complexes*; Pergamon Press: New York, 1962.

16. Jahn H. A.; Teller E. *Proc. R. Soc. Lond. A: Math. Phys. Sci. (1934–1990)* **1937**, *161*, 220.

17. Solomon E. I. *Comments Inorg. Chem.* **1984**, *3*, 225.

18. Gillard R. D. In *Physical Methods in Advanced Inorganic Chemistry*; Hill H. A. O.; Day P., Eds.; Interscience: New York, 1968; p 167.

19. Mason S. F. *Q. Rev. Chem. Soc.* **1963**, *17*, 20.

20. Moffitt W.; Moscowitz A. *J. Chem. Phys.* **1959**, *30*, 648.

21. Moffitt W.; Woodward R. B.; Moscowitz A.; Klyne W.; Djerassi C. *J. Am. Chem. Soc.* 1961, *83*, 4013.

22. Piepho S.; Schatz P. N. *Group Theory in Spectroscopy: With Applications to Magnetic Circular Dichroism*; Wiley: New York, 1983.

23. Buckingham A. D.; Stephens P. J. *Annu. Rev. Phys. Chem.* **1966**, *17*, 399.

24. Thomson A. J.; Cheesman M. R.; George S. J. In *Methods in Enzymology*; Abelson J. N.; Simon M. I.; Riordan J. F.; Vallee B. L., Eds.; Academic Press: New York, 1993; Vol. 226, p 199.

25. Gewirth A. A.; Solomon E. I. *J. Am. Chem. Soc.* **1988**, *110*, 3811.

26. Gerstman B. S.; Brill A. S. *J. Chem. Phys.* **1985**, *82*, 1212.

27. Neese F.; Solomon E. I. *Inorg. Chem.* **1999**, *38*, 1847.

28. Gebhard M. S.; Koch S. A.; Millar M.; Devlin F. J.; Stephens P. J.; Solomon E. I. *J. Am. Chem. Soc.* **1991**, *113*, 1640.

29. Solomon E. I.; Pavel E. G.; Loeb K. E.; Campochiaro C. *Coord. Chem. Rev.* **1995**, *144*, 369.

30. Whittaker J. W.; Solomon E. I. *J. Am. Chem. Soc.* **1988**, *110*, 5329.

31. Johnson M. K. In *Physical Methods in Bioinorganic Chemistry: Spectroscopy and Magnetism*; Que L.,Ed.; University Science Books: New York, **2000**; p 233.

32. Bleaney B.; Abragam A. *Electron Paramagnetic Resonance of Transition Ions*; Clarendon Press: London, 1970.

33. Kramers H. A. *Koninklijke Akad. van Wetenschappen* **1930**, 962.

34. Solomon E. I.; Brunold T. C.; Davis M. I.; Kemsley J. N.; Lee S. K.; Lehnert N.; Neese F.; Skulan A. J.; Yang Y. S.; Zhou J. *Chem. Rev.* **2000**, *100*, 235.

35. Laiho R. *Phys. Status Solidi (b)* **1975**, *69*, 579.

36. Bird B. D.; Day P. *J. Chem. Phys.* **1968**, *49*, 392.

37. Ballhausen C. J.; Gray H. B. In *Frontiers in Chemistry*; Breslow R.; Karplus M., Eds.; W. A. Benjamin, Inc.: New York, 1965.

38. Mulliken R. S.; Rieke C. A.; Orloff D.; Orloff H. *J. Chem. Phys.* **1949**, *17*, 1248.

39. Desjardins S. R.; Penfield K. W.; Cohen S. L.; Musselman R. L.; Solomon E. I. *J. Am. Chem. Soc.* **1983**, *105*, 4590.

40. Baldwin M. J.; Root D. E.; Pate J. E.; Fujisawa K.; Kitajima N.; Solomon E. I. *J. Am. Chem. Soc.* **1992**, *114*, 10421.

41. Ros P.; Schuit G. C. A. *Theor. Chim. Acta* **1966**, *4*, 1.

42. Karpishin T. B.; Gebhard M. S.; Solomon E. I.; Raymond K. N. *J. Am. Chem. Soc.* **1991**, *113*, 2977.

43. Rehr J. J. Ankudinov A. L. *Coord. Chem. Rev.* **2005**, *249*, 131.

44. Sarangi R.; Hocking R. K.; Neidig M. L.; Benfatto M.; Holman T. R.; Solomon E. I.; Hodgson K. O.; Hedman B. *Inorg. Chem.* **2008**, *47*, 11543–11550.

45. Solomon E. I.; Basumallick L.; Chen P.; Kennepohl P. *Coord. Chem. Rev.* **2005**, *249*, 229.

46. Siegbahn K.; Nordling C.; Fahlman R.; Nordberg K. *ESCA: Atomic, Molecular and Solid State Structure Studied by Means of Electron Spectroscopy*; Royal Society of Sciences: Uppsala, 1967.

47. Kau L. S.; Spira-Solomon D. J.; Penner-Hahn J. E.; Hodgson K. O.; Solomon E. I. *J. Am. Chem. Soc.* **1987**, *109*, 6433.

48. Hahn J. E.; Scott R. A.; Hodgson K. O.; Doniach S.; Desjardins S. R.; Solomon E. I. *Chem. Phys. Lett.* **1982**, *88*, 595.

49. Shadle S. E.; Penner-Hahn J. E.; Schugar H. J.; Hedman B.; Hodgson K. O.; Solomon E. I. *J. Am. Chem. Soc.* **1993**, *115*, 767.

50. Solomon E. I.; Szilagyi R. K.; DeBeer George S.; Basumallick L. *Chem. Rev.* **2004**, *104*, 419.

51. Westre T. E.; Kennepohl P.; DeWitt J. G.; Hedman B.; Hodgson K. O.; Solomon E. I. *J. Am. Chem. Soc.* **1997**, *119*, 6297.

52. de Groot F. *Coord. Chem. Rev.* **2005**, *249*, 31.

53. George S. J.; Lowery M. D.; Solomon E. I.; Cramer S. P. *J. Am. Chem. Soc.* **1993**, *115*, 2968.

54. Wasinger E. C.; de Groot F. M.; Hedman B.; Hodgson K. O.; Solomon E. I. *J. Am. Chem. Soc.* **2003**, *125*, 12894.

55. Hocking R. K.; Wasinger E. C.; Yan Y. L.; de Groot F. M. F.; Walker F. A.; Hodgson K. O.; Hedman B.; Solomon E. I. *J. Am. Chem. Soc.* **2007**, *129*, 113.

56. Hocking R. K.; Wasinger E. C.; de Groot F. M. F.; Hodgson K. O.; Hedman B.; Solomon E. I. *J. Am. Chem. Soc.* **2006**, *128*, 10442.

57. Rose K.; Shadle S. E.; Eidsness M. K.; Kurtz D. M.; Scott R. A.; Hedman B.; Hodgson K. O.; Solomon E. I. *J. Am. Chem. Soc.* **1998**, *120*, 10743.

58. Venkateswara Rao P.; Holm R. H. *Chem. Rev.* **2004**, *104*, 527.

59. Rose K.; Shadle S. E.; Glaser T.; de Vries S.; Cherepanov A.; Canters G. W.; Hedman B.; Hodgson K. O.; Solomon E. I. *J. Am. Chem. Soc.* **1999**, *121*, 2353.

60. Glaser T.; Rose K.; Shadle S. E.; Hedman B.; Hodgson K. O.; Solomon E. I. *J. Am. Chem. Soc.* **2001**, *123*, 442.

61. Holm R. H.; Kennepohl P.; Solomon E. I. *Chem. Rev.* **1996**, *96*, 2239.